

This work was written as part of one of the author's official duties as an Employee of the United States Government and is therefore a work of the United States Government. In accordance with 17 U.S.C. 105, no copyright protection is available for such works under U.S. Law.

Public Domain Mark 1.0

<https://creativecommons.org/publicdomain/mark/1.0/>

Access to this work was provided by the University of Maryland, Baltimore County (UMBC) ScholarWorks@UMBC digital repository on the Maryland Shared Open Access (MD-SOAR) platform.

Please provide feedback

Please support the ScholarWorks@UMBC repository by emailing scholarworks-group@umbc.edu and telling us what having access to this work means to you and why it's important to you. Thank you.

JGR Space Physics



RESEARCH ARTICLE

10.1029/2022JA030949

Key Points:

- Temporal, spatial, and velocity-space derivatives of electron phase space density are computed and compared for the first time using the Magnetospheric Multiscale spacecraft
- Single-spacecraft measurements show how parallel electric fields are balanced by electron pressure gradients at Earth's magnetopause
- A simplified form of the electron distribution function provides intuition for interpreting nongyrotropic velocity-space structures

Correspondence to:

J. R. Shuster,
jason.shuster@unh.edu








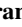














Citation:

Shuster, J. R., Gershman, D. J., Giles, B. L., Bessho, N., Sharma, A. S., Dorelli, J. C., et al. (2023). Temporal, spatial, and velocity-space variations of electron phase space density measurements at the magnetopause. *Journal of Geophysical Research: Space Physics*, 128, e2022JA030949. <https://doi.org/10.1029/2022JA030949>

Received 25 AUG 2022

Accepted 8 MAR 2023

Temporal, Spatial, and Velocity-Space Variations of Electron Phase Space Density Measurements at the Magnetopause

J. R. Shuster^{1,2,3} , D. J. Gershman² , B. L. Giles² , N. Bessho^{1,2} , A. S. Sharma¹, J. C. Dorelli², V. Uritsky^{2,4}, S. J. Schwartz⁵ , P. A. Cassak⁶ , R. E. Denton⁷ , L.-J. Chen² , H. Gurram^{1,2}, J. Ng^{1,2} , J. Burch⁸ , J. Webster⁹ , R. Torbert^{3,8} , W. R. Paterson², C. Schiff², A. F. Viñas^{2,4}, L. A. Avanov^{1,2} , J. Stawarz^{10,11} , T. C. Li⁷ , Y.-H. Liu⁷ , M. R. Argall³ , A. Afshari¹² , D. S. Payne¹³ , C. J. Farrugia³ , J. Verniero², F. Wilder¹⁴, K. Genestreti⁸ , and D. E. da Silva^{2,4,15} 

¹Department of Astronomy, University of Maryland College Park, College Park, MD, USA, ²NASA Goddard Space Flight Center, Greenbelt, MD, USA, ³Space Science Center, University of New Hampshire, Durham, NH, USA, ⁴Department of Physics, Catholic University of America, Washington, DC, USA, ⁵Laboratory for Atmospheric and Space Physics, University of Colorado Boulder, Boulder, CO, USA, ⁶Department of Physics and Astronomy and the Center for KINETIC Plasma Physics, West Virginia University, Morgantown, WV, USA, ⁷Department of Physics and Astronomy, Dartmouth College, Hanover, NH, USA, ⁸Southwest Research Institute, San Antonio, TX, USA, ⁹Department of Physics and Astronomy, Rice University, Houston, TX, USA, ¹⁰Department of Physics, Imperial College London, London, GB, ¹¹Department of Mathematics, Physics, and Electrical Engineering, Northumbria University, Newcastle upon Tyne, UK, ¹²Department of Physics and Astronomy, University of Iowa, Iowa City, IA, USA, ¹³Institute for Research in Electronics and Applied Physics, University of Maryland, College Park, MD, USA, ¹⁴Department of Physics, University of Texas at Arlington, Arlington, TX, USA, ¹⁵Goddard Planetary Heliophysics Institute, University of Maryland Baltimore County, Baltimore County, MD, USA

Abstract Temporal, spatial, and velocity-space variations of electron phase space density are measured observationally and compared for the first time using the four magnetospheric multiscale (MMS) spacecraft at Earth's magnetopause. Equipped with these unprecedented spatiotemporal measurements offered by the MMS tetrahedron, we compute each term of the electron Vlasov equation that governs the evolution of collisionless plasmas found throughout the universe. We demonstrate how to use single spacecraft measurements to improve the resolution of the electron pressure gradient that supports nonideal parallel electric fields, and we develop a model to intuit the types of kinetic velocity-space signatures that are observed in the Vlasov equation terms. Furthermore, we discuss how the gradient in velocity-space sheds light on plasma energy conversion mechanisms and wave-particle interactions that occur in fundamental physical processes such as magnetic reconnection and turbulence.

Plain Language Summary Measuring spatial and temporal variations of space plasmas usually requires choosing between the following two approaches: (a) measure how the quantity of interest changes in time as the plasma flows past a single spacecraft, or (b) compare measurements of the quantity gathered from multiple, spatially separated spacecraft. The first approach requires measurements at two different times from the same spatial location, while the second requires simultaneous measurements taken from multiple spatial points. There are advantages and disadvantages to each of these existing approaches. While single-spacecraft measurements may be gathered at high time resolution, a known limitation of single-point data sets is the inability to distinguish between spatial and temporal variations: both a thin, slow-moving structure and a thick, fast-moving one could produce the same measured time series of a quantity when sampled at only a single spatial location. In many situations, multipoint measurements, such as those provided by NASA's Magnetospheric Multiscale (MMS) four-spacecraft mission enable us to overcome that limitation; however, oftentimes electron-scale structures of interest are even smaller than the close inter-spacecraft separation of MMS, which means typical techniques for estimating spatial gradients from the four spacecraft also become inaccurate for those events. In this paper, we present a new approach for quantifying variations in a collisionless plasma that only requires information about the plasma particles and fields taken at a *single* point in time and space.

1. Introduction

The Vlasov equation provides an established theoretical foundation for kinetic plasma physics and a wide variety of fundamental plasma energization phenomena (e.g., Harris, 1962; Landau, 1946; Nicholson, 1983; Roth

© 2023. The Authors.

This is an open access article under the terms of the Creative Commons Attribution-NonCommercial-NoDerivs License, which permits use and distribution in any medium, provided the original work is properly cited, the use is non-commercial and no modifications or adaptations are made.

et al., 1996; Vlasov, 1945; and references therein). The unprecedented instrumentation onboard NASA's Magnetospheric Multiscale (MMS) mission designed to probe the electron diffusion region (EDR) of magnetic reconnection (e.g., Burch et al., 2016; Torbert et al., 2018) enable direct measurement of each term in the Vlasov equation. Recently, Shuster et al. (2019) established a technique that utilizes the Fast Plasma Investigation (FPI) spectrometers onboard the four MMS spacecraft to directly measure the spatial gradient term of the electron Vlasov equation, $\mathbf{v} \cdot \nabla f_e$. This approach was then adopted to characterize and intuit the velocity-space structure of $\mathbf{v} \cdot \nabla f_e$ in various spatial gradient situations that develop within Earth's dayside magnetopause (Shuster, Gershman, et al., 2021). In this paper, we present and compare MMS measurements of all three terms in the electron Vlasov equation for the first time, including the temporal derivative term $\partial f_e / \partial t$ and the velocity-space gradient term $(\mathbf{F} / m_e) \cdot \nabla_{\mathbf{v}} f_e$, in the context of electron-scale current layers at the magnetopause. Once MMS measurements of each term in the Vlasov equation are obtained, we investigate how those terms balance in velocity-space, a procedure which is a kinetic analog of considering the balance of terms in the electron momentum equation and hence the generalized Ohm's law central to our understanding of the magnetic reconnection process.

The continuity of phase-space density, as stated by the Vlasov equation itself, points to a new approach for quantifying variations in a collisionless plasma that, in principle, only requires knowing the particles' velocity-space structure at a *single* point in time and space. Using data from the suite of FPI spectrometers onboard the MMS tetrahedron, we show how to infer qualitatively equivalent spatiotemporal variations of electron-scale structures from careful measurements of the electron velocity distribution function's *shape* in velocity-space. Rather than suffering from inherent spatial and temporal ambiguities, this approach relies on the third term in the electron Vlasov equation, and thus is limited mainly by the velocity-space resolution of the particle detectors and the accuracy of the electromagnetic field measurements.

For steady-state structures, the primary term in the electron momentum equation capable of balancing a nonideal parallel electric field E_{\parallel} is the parallel component of the electron pressure divergence $(\nabla \cdot \mathbf{P}_e)_{\parallel}$, which is especially difficult to measure for electron-scale structures since the spatial scales involved are commonly smaller than even the close inter-spacecraft separation of MMS. Wilder et al. (2017) reported parallel electric field E_{\parallel} signatures persisting for hundreds of Debye lengths in the context of a symmetric, magnetosheath EDR magnetic reconnection event with a significant guide field. For approximately steady-state structures moving rapidly past the spacecraft, better spatially resolved measurements of the spatial gradient of a quantity along the current sheet normal direction may be estimated by that quantity's temporal derivative. For example, Torbert et al. (2017) applied this technique to explore the normal (N) component of the electron pressure divergence $\nabla_N P_{eNN}$ in an EDR encountered by MMS. In this paper, we develop a method utilizing single-spacecraft $\partial f_e / \partial t$ measurements in the spacecraft frame to probe the kinetic structure of the electrons contributing to $(\nabla \cdot \mathbf{P}_e)_{\parallel}$ to support these types of persistent E_{\parallel} signatures associated with EDRs and the magnetic reconnection process at Earth's magnetopause.

Any quantity obtainable from moments or gradients of the electron velocity distribution function $f_e(\mathbf{v})$ may be explored in velocity-space. Analogously to how taking moments of the kinetic quantities f_e , $\mathbf{v} f_e$, and $(\mathbf{v} - \mathbf{U}_e) f_e$ yields fluid quantities such as density n_e , bulk velocity \mathbf{U}_e , and the pressure tensor \mathbf{P}_e , taking moments of gradients in these kinetic quantities ∇f_e , $\mathbf{v} \cdot \nabla f_e$, and $(\mathbf{F} / m_e) \cdot \nabla_{\mathbf{v}} f_e$ also yields important gradients and physically meaningful fluid quantities, such as: ∇n_e , $\nabla \cdot \mathbf{P}_e$, and $\mathbf{J}_e \cdot \mathbf{E}$, and so on. Understanding the velocity-space structure of each of these quantities deepens our understanding of how fundamental energy conversion processes can operate in a collisionless plasma, which is directly relevant for studies of magnetospheric reconnection, turbulence, and wave-particle interactions such as Landau damping (e.g., Afshari et al., 2021; C. Chen et al., 2019; L.-J. Chen, Hesse, Wang, Bessho, et al., 2016; L.-J. Chen, Hesse, Wang, Gershman, et al., 2016; Genestreti et al., 2018; Gershman et al., 2017; Gurram et al., 2021; Horvath et al., 2020; Li et al., 2019; McCubbin et al., 2022; Ng et al., 2011; Servidio et al., 2017; Sitnov et al., 2018; Shuster et al., 2014, 2015; Stawarz et al., 2021; Wang et al., 2016, 2018; Webster et al., 2018; Yang et al., 2017).

2. Methodology: Computing Electron Phase-Space Density Variations With FPI

In this section, we present our methodology for utilizing FPI Dual Electron Spectrometer (DES) data to compute each derivative of phase space density that appears in the electron Vlasov equation, given by:

$$\frac{df_e}{dt} = \frac{\partial f_e}{\partial t} + \mathbf{v} \cdot \nabla f_e - \frac{e}{m_e} (\mathbf{E} + \mathbf{v} \times \mathbf{B}) \cdot \nabla_{\mathbf{v}} f_e = 0. \quad (1)$$

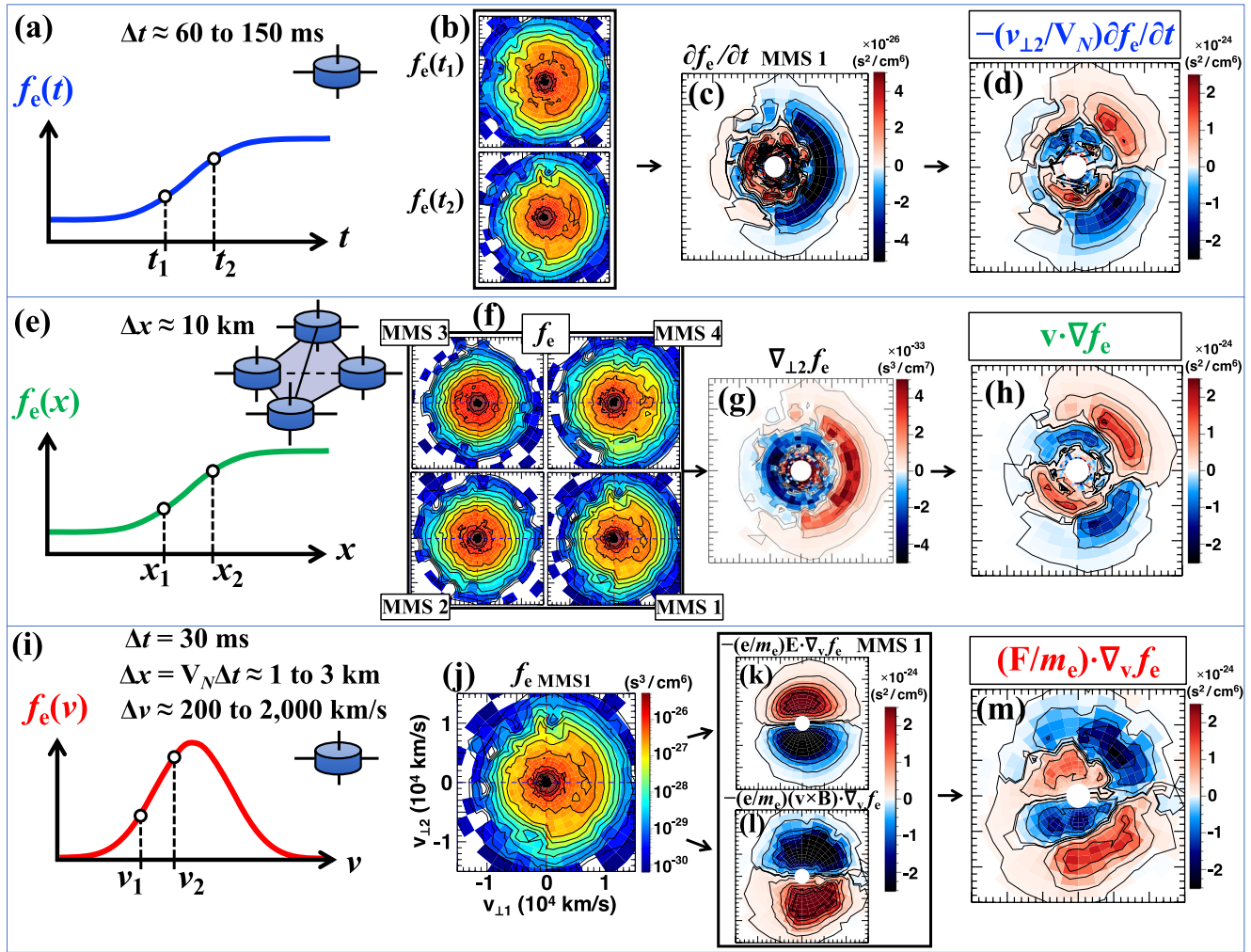


Figure 1. Visualization for the velocity-space balance of each term in the Vlasov equation for the electron-scale current layer observed on 23 December 2016. The three rows illustrate the computation procedure for each term in the electron Vlasov equation: (a)–(d) $\partial f_e / \partial t$, (e)–(h) $\mathbf{v} \cdot \nabla f_e$, and (i)–(m) $(\mathbf{F} / m_e) \cdot \nabla_v f_e$. Panels (a, e, i) show conceptual illustrations of the three distinct ways in which phase space density gradients are computed with magnetospheric multiscale (MMS): (a) the time derivative $\partial f_e / \partial t$ is computed with a single spacecraft using data sampled at multiple points in time, (e) the full spatial gradient term $\mathbf{v} \cdot \nabla f_e$ requires simultaneous measurements from all four, spatially separated spacecraft, and (i) the velocity-space gradient term $(\mathbf{F} / m_e) \cdot \nabla_v f_e$ is computed by combining $f_e(v)$ taken from a single spacecraft at a single point in time and space with the electric (\mathbf{E}) and magnetic (\mathbf{B}) fields measurements. (b) Two electron distribution slices from MMS 1 used to estimate (c) the time derivative $\partial f_e / \partial t$. (d) Using the steady-state assumption (see text for details), the quantity $(-v_{\perp 2} / V_N) \partial f_e / \partial t$ represents a higher spatially resolved version of $\mathbf{v} \cdot \nabla f_e$. (f) Electron distribution slices from all four MMS spacecraft needed to estimate the spatial gradient terms $\nabla_{\parallel} f_e$, $\nabla_{\perp 1} f_e$, and (g) $\nabla_{\perp 2} f_e$. (h) Taking the dot product of the velocity-space coordinate \mathbf{v} with ∇f_e , we obtain the full spatial gradient term $\mathbf{v} \cdot \nabla f_e$. (j) A single electron distribution on which velocity-space gradients are performed and combined with the fields measurements to yield (k) $(-e/m_e) \mathbf{E} \cdot \nabla_v f_e$ and (l) $(-e/m_e) (\mathbf{v} \times \mathbf{B}) \cdot \nabla_v f_e$. (m) Adding the results from (k) and (l) together, we obtain the full velocity-space gradient term $(\mathbf{F} / m_e) \cdot \nabla_v f_e$, which exhibits a velocity-space structure that is qualitatively consistent with (d) $\mathbf{v} \cdot \nabla f_e$ and (h) $\mathbf{v} \cdot \nabla f_e$ as expected from the Vlasov equation. Panel (d) for $(-v_{\perp 2} / V_N) \partial f_e / \partial t$ and (m) for $(\mathbf{F} / m_e) \cdot \nabla_v f_e$ were computed from the four-spacecraft average $\langle f_e \rangle$ for comparison with (h) $\mathbf{v} \cdot \nabla f_e$. Each velocity-space panel represents a slice taken in the $v_{\perp 1}$ - $v_{\perp 2}$ plane.

Figure 1 features a conceptual overview that illustrates each computation technique using the thin, electron-scale current layer observed by MMS on 23 December 2016 reported previously (Shuster, Bessho, et al., 2021; Shuster et al., 2019; Shuster, Gershman, et al., 2021). In the Lagrangian frame following a phase space element, the Vlasov equation states that $df_e/dt = 0$, which corresponds to the physical statement that phase space density is conserved along particle trajectories. In the Eulerian spacecraft frame, however, we must compute each of the partial derivative terms shown above in Equation 1, where we refer the reader to Appendix A for more detailed discussions regarding our computation techniques. Our computational approaches for the three terms $\partial f_e / \partial t$, $\mathbf{v} \cdot \nabla f_e$, and $(-e/m_e) (\mathbf{E} + \mathbf{v} \times \mathbf{B}) \cdot \nabla_v f_e$ are shown sequentially in Figures 1a–1d (top row), Figures 1e–1h (middle row), and Figures 1i–1m (bottom row), respectively. Comparing the rightmost distribution panels shown in Figures 1d, 1h, and 1m, the resulting velocity-space structures are qualitatively similar, even though the

computation approach required to obtain each term is fundamentally different. Computing the time derivative term $\partial f_e / \partial t$ in the MMS frame, we sample f_e at multiple points in time using data from a single spacecraft. For the full spatial gradient term $\mathbf{v} \cdot \nabla f_e$, simultaneous f_e measurements taken from each of the four spacecraft are utilized. Finally, for the velocity space gradient term $-(e/m_e)(\mathbf{E} + \mathbf{v} \times \mathbf{B}) \cdot \nabla_{\mathbf{v}} f_e$, single spacecraft measurements of the distribution f_e from FPI (Pollock et al., 2016), the electric field from the Electric Field Double Probes (EDP) (Ergun et al., 2016; Lindqvist et al., 2016), and magnetic field from the Fluxgate Magnetometer (FGM) (Russell et al., 2016) are required. The following sections explain our approach for computing each term in more detail.

Throughout the paper and for all figures, the distributions shown represent slices in velocity space, and are shown in field-aligned coordinates where v_{\parallel} is parallel to the magnetic field \mathbf{B} , $v_{\perp 1}$ is oriented along $(-\mathbf{U}_e \times \mathbf{B}) \times \mathbf{B}$ (roughly the $\mathbf{E} \times \mathbf{B}$ direction, where \mathbf{E} is the electric field, and \mathbf{U}_e is the electron bulk velocity), and $v_{\perp 2}$ is along $-\mathbf{U}_e \times \mathbf{B}$ (roughly along the direction of \mathbf{E}).

2.1. Temporal Derivative: $\partial f_e / \partial t$

In Figures 2f and 2g, we compare first-order and fourth-order accurate finite difference estimations of the instantaneous time derivative $\partial f_e / \partial t$, where the first-order forward difference expression is given by

$$\frac{\partial f_e}{\partial t} \approx \frac{f_e(t_{i+1}) - f_e(t_i)}{\Delta t}, \quad (2)$$

and the fourth-order central difference expression is given by

$$\frac{\partial f_e}{\partial t} \approx \frac{-f_e(t_{i+2}) + 8f_e(t_{i+1}) - 8f_e(t_{i-1}) + f_e(t_{i-2})}{12\Delta t}, \quad (3)$$

where t_i specifies the i^{th} time index. The full 3D electron velocity distribution function provided by DES is sampled every $\Delta t = 30$ ms, so the total time intervals required to compute the first-order and fourth-order approximations are 60 and 150 ms, respectively. Additionally, because the above estimations require combining f_e measurements gathered at different times, it is important to perform the computations in an inertial frame such as Geocentric Solar Ecliptic (GSE) coordinates, rather than in a time-varying field-aligned coordinate system.

2.2. Spatial Gradient: $\mathbf{v} \cdot \nabla f_e$

We implement the approach recently developed and applied by Shuster et al. (2019) and Shuster, Gershman, et al. (2021) to compute the $\mathbf{v} \cdot \nabla f_e$ term, visually summarized in Figures 1e–1h. The technique used for computing ∇f_e is, in principle, identical to the standard multi-spacecraft approach used to estimate the spatial gradient of any quantity of interest (Harvey, 1998). In general, $f_e(E, \phi, \theta, t)$ is sampled by the four spacecraft at different times and different ϕ locations; thus, we linearly interpolate f_e in time and azimuth to ensure the same region of velocity space is being compared during the four spacecraft gradient estimation. Shuster et al. (2019) include a more detailed discussion of this methodology and make use of the standard deviations for the f_e measurements (Gershman et al., 2015) to estimate the uncertainty of the technique, which is reported to be on the order of 10% of the measurement magnitude. Typical inter-spacecraft separations for MMS are on the order of 10 km. Thus, for electron-scale structures whose thicknesses are significantly smaller than this separation, the four-spacecraft estimate of ∇f_e decreases in accuracy. Nevertheless, following the example of Torbert et al. (2017), in this paper, we present examples of how $\partial f_e / \partial t$ may be used to estimate ∇f_e along the normal direction when there is evidence suggesting the plasma structure passing by the spacecraft is steady-state.

2.3. Velocity-Space Gradient: $(\mathbf{F}/m_e) \cdot \nabla_{\mathbf{v}} f_e$

The velocity-space gradient term requires the most care to compute because data from three instrument suites with different cadences are needed. In this paper, we benchmark the computation technique for two electron-scale current layer encounters: the first is from 23 December 2016 (see Figures 1–4), and the second is from 1 October 2016 (see Figure 5) (see Shuster, Gershman, et al. (2021) for more details about these events). In the last row of Figures 1i–1m, we show intermediate steps of the computation, including velocity-space slices of the contribution from the electric and magnetic field terms, $-(e/m_e)\mathbf{E} \cdot \nabla_{\mathbf{v}} f_e$ and $-(e/m_e)(\mathbf{v} \times \mathbf{B}) \cdot \nabla_{\mathbf{v}} f_e$, which add together to create the self-consistent quadrupolar structure needed to balance the $\mathbf{v} \cdot \nabla f_e$ term. To help reduce the uncertainty

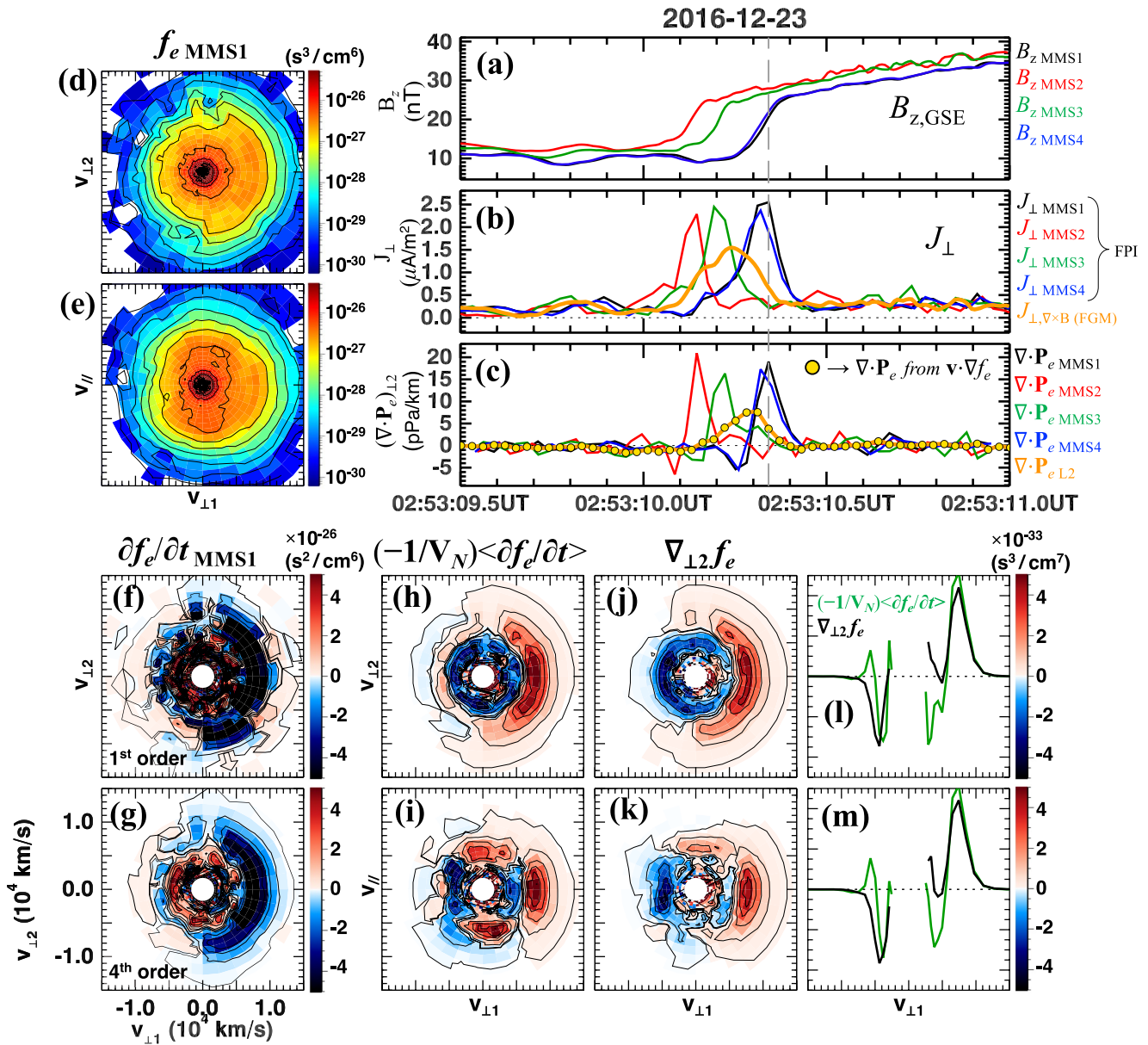


Figure 2. Single-spacecraft measurements of ∇f_e and $\nabla \cdot \mathbf{P}_e$ obtained from $\partial f_e / \partial t$. (a)–(c) Four-spacecraft measurements of relevant plasma properties for the event presented in Figure 1: (a) z -component of the magnetic field in Geocentric Solar Ecliptic (GSE) coordinates, (b) perpendicular current density $\mathbf{J} = en(\mathbf{U}_i - \mathbf{U}_e)$ computed from Fast Plasma Investigation (FPI) moments data for each spacecraft, and $\mathbf{J} = \nabla \times \mathbf{B} / \mu_0$ using the curlometer technique with Fluxgate Magnetometer (FGM) data (orange trace), and (c) \perp -component of the standard four-spacecraft electron pressure divergence $\nabla \cdot \mathbf{P}_e$ (orange trace), along with the single-spacecraft versions of $\nabla \cdot \mathbf{P}_e$ obtained from integrating $\partial f_e / \partial t$ as described in Section 3.1. The gold circles in (c) benchmark our moments procedure, showing how the integral quantity $m_e \int v_{\perp 2} (\mathbf{v} \cdot \nabla f_e) d^3v$ matches almost exactly with the standard measure of $(\nabla \cdot \mathbf{P}_e)_{\perp 2}$. (d, e) Electron velocity distribution slices in the (d) $v_{\perp 1}$ – $v_{\perp 2}$ and (e) $v_{\perp 1}$ – v_{\parallel} planes taken from the time indicated by the dashed line in panels (a)–(c). (f, g) $v_{\perp 1}$ – $v_{\perp 2}$ slices of the temporal derivative $\partial f_e / \partial t$ computed via (f) first order and (g) fourth order finite difference estimation procedure. (h, i) $v_{\perp 1}$ – $v_{\perp 2}$ and (i) $v_{\perp 1}$ – v_{\parallel} slices of the four spacecraft average $(-1/V_N) \langle \partial f_e / \partial t \rangle$ for comparison with (j, k) analogous slices of the standard four-spacecraft measurement of the spatial gradient term $\nabla_{\perp 2} f_e$. (l, m) 1D cuts of $(-1/V_N) \langle \partial f_e / \partial t \rangle$ and $\nabla_{\perp 2} f_e$ along $v_{\perp 1}$ at $v_{\perp 2} = 0$ for quantitative comparison.

arising from performing the velocity-space derivative ∇_v operation, we first smooth the distribution. We then implement fourth-order centered difference derivative estimations to obtain the necessary velocity-space derivative components (see Appendix A for more details of the computation procedure). We perform the computation using two different approaches: the first is performed with respect to the $\{E, \theta, \phi\}$ coordinates native to the FPI detectors, and the second is obtained after interpolating the distribution to a Cartesian velocity-space grid $\{v_x, v_y, v_z\}$. The results of both approaches are qualitatively consistent, and are presented side by side in Figure 4. We note

that the electric and magnetic fields are averaged to the DES 30 ms resolution to arrive at the final expression for the velocity-space gradient term that appears in the Vlasov equation.

3. Balance of Terms in the Electron Vlasov Equation at the Magnetopause

In this section, we compare the velocity-space structure of all three terms in the electron Vlasov equation. This comparison is analogous to investigating the balance of terms in the generalized Ohm's law, which can be derived from taking the first moment of the ion and electron Vlasov equations, except that in this work, we are exploring the balance of each term throughout the entire 3D velocity-space accessible to the FPI spectrometers.

3.1. Single Spacecraft $\nabla \cdot \mathbf{P}_e$ Measurements Obtained From $\partial f_e / \partial t$

We immediately see from Figure 1c that throughout velocity space, $\partial f_e / \partial t$ (colorbar maximum is $10^{-26} \text{ s}^2/\text{cm}^6$) is roughly 2 orders of magnitude smaller than the $\mathbf{v} \cdot \nabla f_e$ term (Figure 1b) and the $(\mathbf{F}/m_e) \cdot \nabla f_e$ term (Figure 1m) (colorbar maximum is $10^{-24} \text{ s}^2/\text{cm}^6$), as noted by Shuster, Gershman, et al. (2021) who focused on the steady-state Vlasov equation (i.e., assuming $\partial f_e / \partial t \approx 0$). Now that we can directly compare measurements of $\partial f_e / \partial t$ to $\mathbf{v} \cdot \nabla f_e$, we are in a position to clarify this result with additional nuance that is required to properly understand the physical situation and account for the MMS observations. For the purposes of the simplified $\mathbf{v} \cdot \nabla f_e$ model developed by Shuster, Gershman, et al. (2021), it was reasonable to neglect the relatively small $\partial f_e / \partial t$ term entirely. However, in Figure 1c, we clearly see that $\partial f_e / \partial t$ exhibits a well-resolved, crescent-shaped structure. Furthermore, multiplying $\partial f_e / \partial t$ by the quantity $(-v_{\perp 2}/V_N)$ (which will be explained below) as we do in Figure 1d, we recover a velocity-space structure comparable both in shape and magnitude to the other two Vlasov equation terms. Thus, we need not ignore $\partial f_e / \partial t$, since evidently this term holds important physical information to convey, along with a useful data product to offer.

Returning to the steady-state assumption of (Shuster, Gershman, et al., 2021), we express the relationship between $\partial f_e / \partial t$, ∇f_e , and $\mathbf{v} \cdot \nabla f_e$ as follows.

$$\frac{Df_e}{Dt} \equiv \frac{\partial f_e}{\partial t} + \mathbf{V}_{str} \cdot \nabla f_e \approx 0 \rightarrow -V_N \frac{\partial f_e}{\partial x_N} \approx \frac{\partial f_e}{\partial t} \quad (4)$$

$$|\mathbf{v} \cdot \nabla f_e| \gg \left| \frac{\partial f_e}{\partial t} \right|, \quad (5)$$

where $\partial f_e / \partial t$ is the time derivative in the spacecraft frame, and the convective derivative notation Df_e/Dt indicates a time derivative of f_e as would be observed in a frame moving with the current layer's structure velocity, $\mathbf{V}_{str} = V_N \hat{\mathbf{x}}_N$. For the events considered here, the typical structure velocity ranges from about $V_N \approx 50$ –100 km/s, whereas the typical electron thermal speed at the magnetopause is on the order of $v_{th,e} \approx 1,000$ –10,000 km/s. Thus, for the electron velocity space coordinates \mathbf{v} measurable with FPI, we arrive at the statement in Equation 5 because $|\mathbf{v}| \gg |V_N|$. Nevertheless, Equation 4, which is valid for steady-state structures, suggests a technique for using $\partial f_e / \partial t$ to approximate $\partial f_e / \partial x_N$ and hence $\mathbf{v} \cdot \nabla f_e$ whenever the following reasoning is valid:

$$\mathbf{v} \cdot \nabla f_e \approx v_N \partial f_e / \partial x_N \approx (-v_N / V_N) \partial f_e / \partial t, \quad (6)$$

where v_N is the velocity-space coordinate in the direction of the spatial gradient. Equation 6 is a good approximation for the events considered here and in several previous studies (Shuster, Bessho, et al., 2021; Shuster et al., 2019; Shuster, Gershman, et al., 2021). The notable advantage offered by Equation 6 is that, for some cases, when the structure velocity \mathbf{V}_{str} is mostly aligned with the gradient direction, then we are permitted to use $(-v_N / V_N) \partial f_e / \partial t$ as a proxy for $\mathbf{v} \cdot \nabla f_e$. In other words, we may effectively trade the spatial resolution of $\mathbf{v} \cdot \nabla f_e$ for the temporal resolution of $\partial f_e / \partial t$. Because DES samples f_e every 30 ms, and typical structure velocities are on the order of 50–100 km/s, then the 30 ms temporal resolution translates to roughly 1–3 km spatial resolution, for example, $(50 \text{ km/s}) \times (0.03 \text{ s}) = 1.5 \text{ km}$. Compared to the typical 10 km inter-spacecraft separation that usually constrains the validity of ∇f_e , the resolution offered by $\partial f_e / \partial t$ for steady-state structures constitutes an order of magnitude increase in spatial resolution. If, however, the structure of interest propagates nearly perpendicularly to the gradient direction, then $\mathbf{V}_{str} \cdot \nabla f_e$ will be too small to make use of this procedure. Additionally, with an inter-spacecraft separation of 10 km and DES cadence of 30 ms, electron-scale structures moving past the spacecraft at velocities V_N exceeding roughly 300 km/s also would not be sufficiently resolved by this approach.

Evidence for the validity of Equations 4–6 is presented in Figure 2 (compare Figures 2h and 2j), where we see that $(-1/V_N)\partial f_e/\partial t$ qualitatively agrees with previously reported MMS measurements of the velocity-space structure of $\nabla_{\perp 2} f_e$. In this figure, we explore the \perp_2 -component of the electron pressure divergence $\nabla \cdot \mathbf{P}_e$ obtained from taking moments of the $(-v_N/V_N)\partial f_e/\partial t$ measurements, where here $v_{\perp 2} \approx v_N$ points roughly along the $\hat{\mathbf{x}}_{\text{GSE}}$ direction. The three panels in Figures 2a–2c show the structure of the current layer as encountered by the four spacecraft. In Figure 2c, we benchmark our integration method by demonstrating that $(\nabla \cdot \mathbf{P}_e)_{\perp 2}$ obtained from taking the first moment of the term $\mathbf{v} \cdot \nabla f_e$ (gold circles) matches $(\nabla \cdot \mathbf{P}_e)_{\perp 2}$ obtained in the standard way by computing the four-spacecraft gradients of FPI's Level 2 (L2) moment quantities (orange trace). This excellent agreement arises essentially due to an exchange in the order of operations for computing $(\nabla \cdot \mathbf{P}_e)_{\perp 2}$: first integrating the distribution to obtain pressure moments followed by taking the spatial gradient of those moments yields the same result as first differentiating the distribution itself and then integrating the result. Additionally, we show the single-spacecraft versions of $(\nabla \cdot \mathbf{P}_e)_{\perp 2}$ obtained by:

$$(\nabla \cdot \mathbf{P}_e)_{\perp 2} \approx m_e \int v_{\perp 2} (\mathbf{v} \cdot \nabla f_e) d^3 v \approx m_e \int v_{\perp 2} \left(\frac{-v_{\perp 2}}{V_N} \right) \frac{\partial f_e}{\partial t} d^3 v = \left(\frac{-1}{V_N} \right) \frac{\partial P_{e\perp 2, \perp 2}}{\partial t}, \quad (7)$$

where we note that for the events considered here, the contribution from the inertial term $\nabla \cdot (m_e n_e \mathbf{U}_e \mathbf{U}_e)$ is negligible, consistent with the results discussed by Shuster et al. (2019).

These single-spacecraft measures of $(\nabla \cdot \mathbf{P}_e)_{\perp 2}$ are better spatially resolved than the four-spacecraft version, which significantly underestimates the magnitude of $(\nabla \cdot \mathbf{P}_e)_{\perp 2}$ because the current layer thickness is less than the spacecraft separation. Measuring $(\nabla \cdot \mathbf{P}_e)_{\perp 2}$ from each spacecraft reveals a distinct bipolar signature that self-consistently works to balance the normal electric field known to develop in asymmetric current layers (e.g., Bessho et al., 2016, 2017). The previously reported electron pressure divergence computed in the standard way from the four spacecraft was found to contribute at most 30% to the force balance within this electron-scale current layer (Shuster et al., 2019). The single-spacecraft measure of $\nabla \cdot \mathbf{P}_e$ that we compute here by taking moments of the term $(-1/V_N)\partial f_e/\partial t$ is found to be 3–4 times larger than the previously reported results, which significantly modifies our understanding about the balance of the terms in the electron momentum equation and generalized Ohm's law for these thin, electron-scale current structures.

Comparing the velocity-space structure of the $(-1/V_N)\partial f_e/\partial t$ term to $\nabla_{\perp 2} f_e$, the perpendicular slice in $v_{\perp 1}$ – $v_{\perp 2}$ exhibits consistency, while the v_{\parallel} – $v_{\perp 1}$ slice reveals an additional signal in the $-v_{\parallel}$ direction that was not resolved by the four-spacecraft measurements (compare Figures 2i and 2k). In the following paragraphs, we discuss the implications of this additional v_{\parallel} feature and the effect it has on $(\nabla \cdot \mathbf{P}_e)_{\parallel}$. For a sustained E_{\parallel} to be balanced in a steady-state 1D current layer, there must be some contribution from $\nabla \cdot \mathbf{T}_e$ or $\nabla \cdot \mathbf{T}_i$ in order for the plasma to maintain quasineutrality, which can be seen by considering the parallel components of the electron and ion momentum equations (using $n = n_i \approx n_e$):

$$E_{\parallel} = \frac{(\nabla \cdot \mathbf{P}_i)_{\parallel}}{en} = -\frac{(\nabla \cdot \mathbf{P}_e)_{\parallel}}{en}. \quad (8)$$

If we attempt to impose the constraint $\nabla \cdot \mathbf{P}_e = \mathbf{T}_e \cdot \nabla n_e$ and $\nabla \cdot \mathbf{P}_i = \mathbf{T}_i \cdot \nabla n_i$ along with the requirement that $\nabla \rightarrow \partial/\partial x_{\perp 2}$, then Equation 8 cannot be satisfied because the resulting ion and electron terms have different signs. Analogously to Equation 7, we obtain $(\nabla \cdot \mathbf{P}_e)_{\parallel}$ from $\partial f_e/\partial t$ via the approximation:

$$(\nabla \cdot \mathbf{P}_e)_{\parallel} \approx m_e \int v_{\parallel} (\mathbf{v} \cdot \nabla f_e) d^3 v \approx m_e \int v_{\parallel} \left(\frac{-v_{\perp 2}}{V_N} \right) \frac{\partial f_e}{\partial t} d^3 v = \left(\frac{-1}{V_N} \right) \frac{\partial P_{e\parallel, \perp 2}}{\partial t}. \quad (9)$$

This single spacecraft measure of the parallel component of the electron pressure divergence (see the green traces in Figures 3c and 3d) exhibits qualitative agreement with the parallel electric field E_{\parallel} (black traces), whereas the standard four-spacecraft measure of $(\nabla \cdot \mathbf{P}_e)_{\parallel}$ shows no such agreement. We note that the higher frequency fluctuations in E_{\parallel} detected by EDP later in the interval are not captured by the FPI measurements because the frequency of those variations is higher than the DES cadence.

The $v_{\perp 1}$ – $v_{\perp 2}$ slices of f_e observed by MMS 2 (Figure 3, panels A1–A3) exhibit an electron crescent-shaped structure, similar to that observed by MMS 1 (see Figures 2d and 2e). The velocity-space structure of $(-1/V_N)\partial f_e/\partial t$ and $(-v_{\perp 2}/V_N)\partial f_e/\partial t$ in the $v_{\perp 1}$ – $v_{\perp 2}$ plane (Figure 3, panels B1–B3, and C1–C3) exhibit similar crescent and quadrupole structures as those modeled in Shuster, Gershman, et al. (2021), except here the effective spatial resolution for calculating ∇f_e is improved (about 1 km instead of 10 km). The bipolar velocity-space signature along $v_{\perp 1}$ at t_1 in B1 seen as

MMS enters the layer is consistent with a bulk velocity gradient ∇U_e signature. At the maximum $(\nabla \cdot \mathbf{P}_e)_{\parallel}$ at time t_2 , distribution B2 exhibits a more complicated, elongated crescent structure. As MMS exits the layer, the distribution slice in B3 is reversed in polarity compared to B1. At the E_{\parallel} peak (time t_2), the v_{\parallel} - $v_{\perp 12}$ slice of f_e (panel D2) shows an enhanced, asymmetric electron population in the lower left quadrant ($v_{\parallel} < 0$ and $v_{\perp 12} < 0$). The presence of this electron population skews the distribution and contributes to the off-diagonal element of the electron pressure tensor $P_{e\parallel 12}$, the gradient of which acts to support E_{\parallel} within the layer. The corresponding velocity-space structures of $(-1/V_N)\partial f_e/\partial t$ and $(-v_{\perp 12}/V_N)\partial f_e/\partial t$ in the $v_{\perp 11}$ - $v_{\perp 12}$ plane (Figure 3, panels E1–E3, and F1–F3) show which electrons contribute to the $\nabla \cdot \mathbf{P}_e$ moment to self-consistently balance the sustained E_{\parallel} . In particular, panels E2 and E3 show a region of velocity space in the lower left quadrant featuring an asymmetric enhancement with $(-1/V_N)\partial f_e/\partial t > 0$ (red color), corresponding to the electron population in $v_{\parallel} < 0$ and $v_{\perp 12} < 0$ that emerges when taking the difference of distributions D2 and D3. Multiplying by the velocity-space coordinate $v_{\perp 12}$, we obtain the structures in panels F1 through F3, which contribute directly to $(\nabla \cdot \mathbf{P}_e)_{\parallel}$ upon integrating over velocity space. Both panels F2 and F3 show a surplus of unbalanced negative (blue) pixels, which result in the $-(\nabla \cdot \mathbf{P}_e)_{\parallel} < 0$ signature in panel (d) at times t_2 and t_3 needed to support $E_{\parallel} < 0$. Panel F1 exhibits a more symmetric structure, which is why $(\nabla \cdot \mathbf{P}_e)_{\parallel}/(en_e)$ is nearly 0 at time t_1 .

For comparison to the MMS 2 measurements, panels G1–G3 show f_e as observed by MMS 1, along with the corresponding spatial gradient term $\nabla_{\perp 12} f_e$ computed from the four spacecraft, at times t_4 , t_5 , and t_6 (panels H1–H3). Although the spatial resolution of the four-spacecraft $\nabla_{\perp 12} f_e$ is not as well-resolved compared to the quantities obtained from $\partial f_e/\partial t$ discussed above, there is still a discernible pattern corresponding to local gradients in the electron temperature components. These distinct structures readily seen in panels H1 and H3 correspond to spatial gradients in the perpendicular and parallel electron temperatures, respectively, as indicated by the schematics in Figures 3e and 3g. The middle diagram in Figure 3f illustrates the polarity of a cut along the $v_{\perp 12}$ -direction (for Figure 3e) or the v_{\parallel} -direction (for Figure 3g), indicative of how the spatial gradient in the distribution's temperature operates to effect the tripolar velocity-space peaks in $\nabla_{\perp 12} f_e$.

3.2. Comparing the First Measurements of $(\mathbf{F}/m_e) \cdot \nabla_{\mathbf{v}} f_e$ to $\mathbf{v} \cdot \nabla f_e$ and $\partial f_e/\partial t$

In this section, we discuss the first measurements of $(\mathbf{F}/m_e) \cdot \nabla_{\mathbf{v}} f_e$ with MMS, and we present a comparison of the velocity-space structure of each term in the electron Vlasov equation to assess the consistency of the gradient calculations. Figure 4 illustrates each step required to compute the full $(\mathbf{F}/m_e) \cdot \nabla_{\mathbf{v}} f_e$ term with MMS. For context, the uppermost panel (Figure 4a) shows four spacecraft measurements of the perpendicular electron bulk velocity $U_{e\perp 1}$ with times t_1 and t_2 indicating the times at which the $v_{\perp 11}$ - $v_{\perp 12}$ distribution slices below are taken. The second panel (Figure 4b) shows the balance of the dominant terms in the electron momentum equation. Because the thickness of the current layer is smaller than the spacecraft separation, the single-spacecraft measure of $(\nabla \cdot \mathbf{P}_e)_{\perp 12}$ (blue trace) balances best with the force density $en_e(\mathbf{E} + \mathbf{U}_e \times \mathbf{B})$ (orange trace), whereas the standard four-spacecraft measure of $(\nabla \cdot \mathbf{P}_e)_{\perp 12}$ (green trace) is broadened and reduced in magnitude. We compute the first moment of $(\mathbf{F}/m_e) \cdot \nabla_{\mathbf{v}} f_e$ (gold circles), which exhibits excellent agreement with the force density term $en_e(\mathbf{E} + \mathbf{U}_e \times \mathbf{B})$ (orange trace), as expected (see Equation A28 in Appendix A).

The $(-e/m_e)E_{\parallel}\partial f_e/\partial v_{\parallel}$ term (Figure 4a) is related to the instantaneous measure of the field-particle correlation (FPC) indicating local energization by E_{\parallel} (see e.g., McCubbin et al. (2022)). For this event, E_{\parallel} is small compared to $E_{\perp 12}$, so the signal in $(-e/m_e)E_{\parallel}\partial f_e/\partial v_{\parallel}$ (Figure 4a) appears faint compared to $(-e/m_e)E_{\perp 12}\partial f_e/\partial v_{\perp 12}$ (Figure 4b). Thus, the full term $(-e/m_e)\mathbf{E} \cdot \nabla_{\mathbf{v}} f_e$ in Figure 4c (computed in spherical energy-space coordinates) and Figure 4d (computed in Cartesian coordinates) closely resemble the structure in $(-e/m_e)E_{\perp 12}\partial f_e/\partial v_{\perp 12}$. The $(-e/m_e)(\mathbf{v} \times \mathbf{B}) \cdot \nabla_{\mathbf{v}} f_e$ term (Figure 4g) is directly proportional to the gyrophase derivative $\partial f_e/\partial \phi_g$ (e.g., Gurnett & Bhattacharjee, 2005), and is written simply as:

$$(-e/m_e)(\mathbf{v} \times \mathbf{B}) \cdot \nabla_{\mathbf{v}} f_e = -\omega_{ce} \left(v_{\perp 12} \frac{\partial f_e}{\partial v_{\perp 11}} - v_{\perp 11} \frac{\partial f_e}{\partial v_{\perp 12}} \right) = \omega_{ce} \frac{\partial f_e}{\partial \phi_g}, \quad (10)$$

where ϕ_g denotes the gyrophase angle related to the velocity-space coordinates by: $\tan(\phi_g) = v_{\perp 12}/v_{\perp 11}$, and $\omega_{ce} = eB/m_e$ is the electron cyclotron frequency. The two intermediate terms $-\omega_{ce}v_{\perp 12}\partial f_e/\partial v_{\perp 11}$ and $-\omega_{ce}v_{\perp 11}\partial f_e/\partial v_{\perp 12}$ are shown in Figures 4e and 4f, respectively. Alternatively, the Cartesian analog (Figure 4h) is computed in GSE coordinates (see Appendix A) as follows:

$$(-e/m_e)(\mathbf{v} \times \mathbf{B}) \cdot \nabla_{\mathbf{v}} f_e = (-e/m_e) \left[(v_y B_z - v_z B_y) \frac{\partial f_e}{\partial v_x} + (v_z B_x - v_x B_z) \frac{\partial f_e}{\partial v_y} + (v_x B_y - v_y B_x) \frac{\partial f_e}{\partial v_z} \right]. \quad (11)$$

The last two rows of Figure 4 show comparisons of all three terms of the electron Vlasov equation measured by MMS 2 at time t_1 (panels i–l) and the four-spacecraft average at time t_2 (panels m–p), where the two times are indicated in the upper panel of the electron bulk velocity $U_{e\perp 1}$ observed by the four spacecraft. The slice in Figure 4j shows the measure of $\mathbf{v} \cdot \nabla f_e$ obtained from $(v_{\perp 2}/V_N)\partial f_e/\partial t$ (discussed above), while for comparison, the slice in Figure 4n shows the full $\mathbf{v} \cdot \nabla f_e$ term obtained from the standard four spacecraft spatial gradient. All quantities in the second to last row (panels i–l) feature single-spacecraft computations at MMS 2, while quantities in the last row of Figure 4 (panels m–p) are averaged over the MMS tetrahedron. Comparing Figures 4n and 4p (which correspond to Figures 1h and 1m, respectively), there is notable qualitative agreement that is consistent with the electron Vlasov equation: since the magnitude of $\partial f_e/\partial t$ is negligible compared to $\mathbf{v} \cdot \nabla f_e$ and $(\mathbf{F}/m_e) \cdot \nabla_{\mathbf{v}} f_e$ throughout velocity-space, we expect the regions of positive red (negative blue) pixels in $\mathbf{v} \cdot \nabla f_e$ to be balanced by regions of negative blue (positive red) pixels in $(\mathbf{F}/m_e) \cdot \nabla_{\mathbf{v}} f_e$. While there is qualitative agreement between these regions of velocity space, quantitative agreement appears to be lacking due to the differing relative sizes of the velocity-space regions of alternating color; this disagreement, which we suspect is due to instrumental limitations, is revisited below.

Next, we consider the temporal evolution and velocity-space balance of these structures in each term of the electron Vlasov equation by considering another electron-scale current layer encountered by MMS on 1 October 2016 (see Shuster, Gershman, et al. (2021) for additional discussion of this event). Figures 5a–5c provide the plasma context for this event, along with a sequence of five times (indicated by gray dashed lines) that correspond to the time each column of $v_{\perp 1}$ – $v_{\perp 2}$ distribution slices (1–5) was taken. The first row of distribution slices (A1–A5) shows the nongyrotropic structure of f_e throughout the layer as observed by MMS 3. Distributions A2 and A3 feature a crescent-type structure, while the distribution becomes more elliptical along the $v_{\perp 2}$ direction in distribution A4.

The second row (B1–B5) features the time derivative term $\partial f_e/\partial t$ from MMS 3. Again, $\partial f_e/\partial t$ is roughly 2 orders of magnitude smaller throughout velocity space compared to the other Vlasov equation terms, consistent with Equations 4 and 5. The bipolar pattern in $\partial f_e/\partial t$ seen in distribution B4 is consistent with the signature corresponding to a local bulk velocity gradient $\nabla_{\perp 2} U_{e\perp 1}$ discussed previously (see figs. 1e and 3 of Shuster, Gershman, et al. (2021)). Distributions B2 and B3 show more complicated, nested structures yielding a tripolar pattern (blue, red, and blue) going along the $v_{\perp 1}$ direction at $v_{\perp 2} \approx 0$. Distributions (C1–C5) show the full term $\mathbf{v} \cdot \nabla f_e$ computed from the four spacecraft. Since this quantity is effectively an average over the MMS tetrahedron, its magnitude is reduced compared to the single-spacecraft measurements in rows D and E. This four-spacecraft measure of $\mathbf{v} \cdot \nabla f_e$ does capture some of the nested distribution structures in distributions C2 and C3; however, the signatures are not as pronounced as those seen in row D.

In distributions (D1–D5), we make use of Equation 6 to obtain a better spatially resolved version of $\mathbf{v} \cdot \nabla f_e$ via the quantity $(-v_{\perp 2}/V_N)\partial f_e/\partial t$. The magnitude of this quantity based on this single-spacecraft measure of $\partial f_e/\partial t$ is comparable to the $(\mathbf{F}/m_e) \cdot \nabla_{\mathbf{v}} f_e$ term, and reflects the more detailed velocity-space signatures. Distribution D2 contains at least six distinct regions of alternating color: going from left to right along $v_{\perp 1}$, there are three regions alternating from blue \rightarrow red \rightarrow blue for $v_{\perp 2} > 0$, and the mirror image red \rightarrow blue \rightarrow red for $v_{\perp 2} < 0$. Distributions (E1–E5) show the full $(\mathbf{F}/m_e) \cdot \nabla_{\mathbf{v}} f_e$ term computed following the procedure outlined and discussed in Figure 4. The magnitudes of $(\mathbf{F}/m_e) \cdot \nabla_{\mathbf{v}} f_e$ in this row are mostly reversed from the structures in the row just above it, as expected from the Vlasov equation. Distributions E2 and E3 also capture the six distinct regions of alternating polarity in velocity space comparable to distributions D2 and D3. Finally, row F estimates the balance between these two most prominent terms shown in rows D and E by computing the quantity: $(v_{\perp 2}/V_N)\partial f_e/\partial t - (\mathbf{F}/m_e) \cdot \nabla_{\mathbf{v}} f_e$. Due to the varying spatiotemporal and velocity-space instrument resolutions affecting both terms in this difference, the result is somewhat noisy. Nevertheless, the magnitude and coherency of row F are visibly muted from the pronounced and distinct structures featured in the individual terms $(-v_{\perp 2}/V_N)\partial f_e/\partial t$ and $(\mathbf{F}/m_e) \cdot \nabla_{\mathbf{v}} f_e$ in rows D and E, which reflects qualitative consistency with expectations based on the Vlasov equation.

3.3. Double-Maxwellian Model for the Balance of $\mathbf{v} \cdot \nabla f_e$ and $(\mathbf{F}/m_e) \cdot \nabla_{\mathbf{v}} f_e$

In this section, we develop a model that offers an intuition for interpreting the balance between $\mathbf{v} \cdot \nabla f_e$ and $(\mathbf{F}/m_e) \cdot \nabla_{\mathbf{v}} f_e$ in the electron Vlasov equation. Previously, Shuster, Gershman et al. (2021) developed a simplified model (see their Equation 1) based on a single Maxwellian population that captured the observed variations in $\mathbf{v} \cdot \nabla f_e$ for various kinds of electron-scale gradient situations arising at the Earth's magnetopause, including

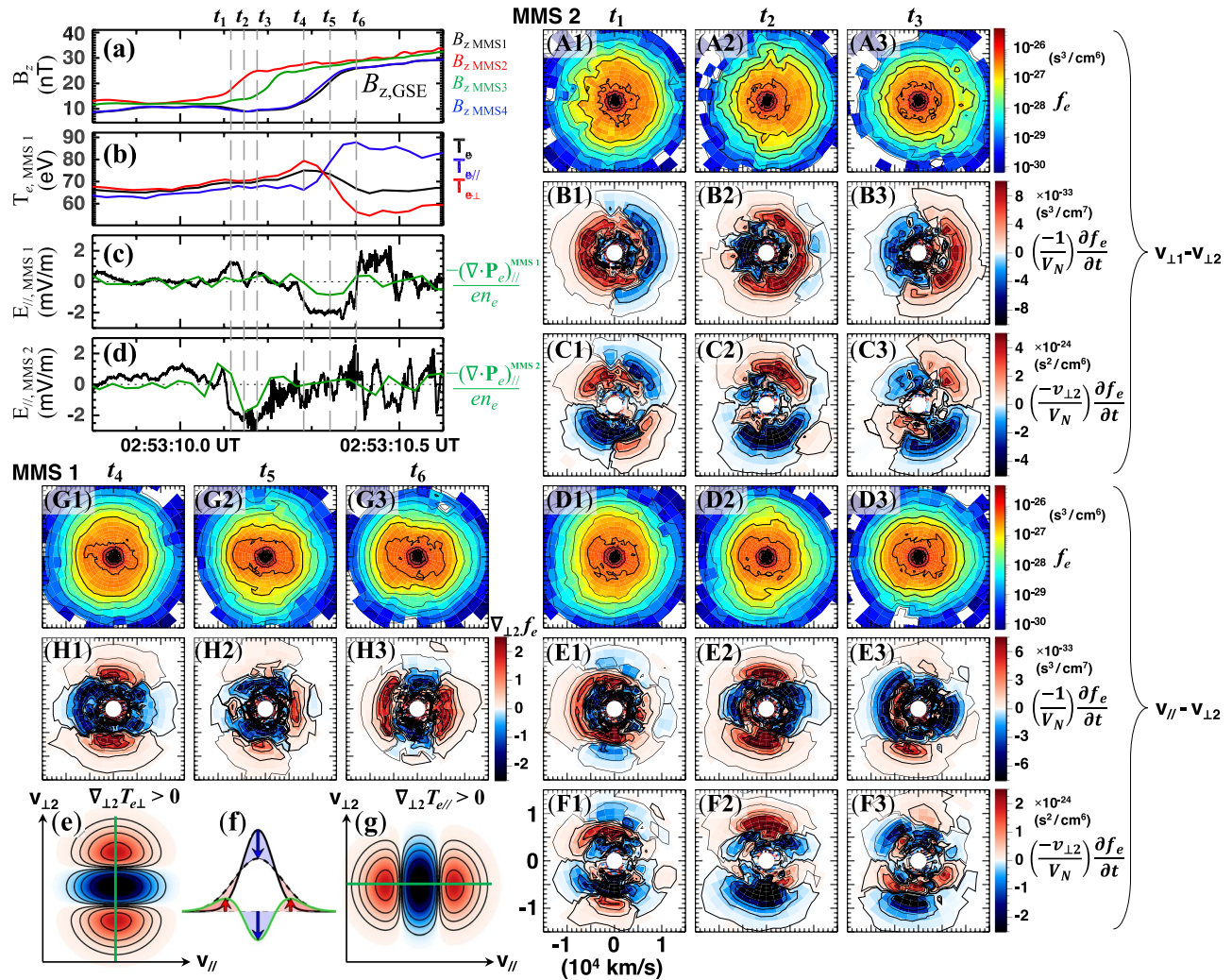


Figure 3. Single-spacecraft measurements of the parallel component of the electron pressure divergence $(\nabla \cdot \mathbf{P}_e)_\parallel$ obtained from $\partial f_e / \partial t$ agree with the large-scale parallel electric field E_\parallel detected by Electric Field Double Probe (EDP) for the 23 December 2016 event. (a) Magnetic field Geocentric Solar Ecliptic (GSE) z -component observed by all four magnetospheric multiscale (MMS) spacecraft. (b) Total (black), parallel (blue), and perpendicular (red) electron temperature profiles from MMS 1. (c, d) Parallel electric field from EDP (black) and single-spacecraft measure of $(-\nabla \cdot \mathbf{P}_e)_\parallel / (en_e)$ computed from FPI measurements of $\partial f_e / \partial t$ as defined in the text (green) for MMS 1 and 2, respectively. Rows A through F show MMS 2 distribution slices taken from times t_1 , t_2 , and t_3 as indicated by the dashed lines in panels (a)–(d). (A1–A3) $v_{\perp 1}-v_{\perp 12}$ slices of f_e showing the spatial evolution of the crescent-shaped velocity-space structure. (B1–B3) and (C1–C3) feature single-spacecraft measurements of $(-1/V_N) \partial f_e / \partial t$ and $(-v_{\perp 12}/V_N) \partial f_e / \partial t$ that are representative of increased spatial resolution versions of $\nabla_{\perp 12} f_e$ and $\mathbf{v} \cdot \nabla f_e$, respectively. (D1–D3), (E1–E3), and (F1–F3) show $v_{\parallel}-v_{\perp 12}$ slices of the same quantities as (A1–A3), (B1–B3), and (C1–C3), respectively, showing the kinetic velocity-space structures which contribute directly to the $(\nabla \cdot \mathbf{P}_e)_\parallel$ that supports the large-scale E_\parallel . Row G shows MMS 1 $v_{\parallel}-v_{\perp 12}$ slices of f_e from times t_4 , t_5 , and t_6 , the times when MMS 1 observed the E_\parallel structure. For reference, Row H shows the four-spacecraft measurement of $\nabla_{\perp 12} f_e$, which has a lower spatial resolution (average spacecraft separation is approximately 10 km), yet still exhibits distinct velocity-space patterns corresponding to the spatial gradient in the parallel and perpendicular electron temperatures as indicated by the schematics in panels (e), (f), and (g).

density, bulk velocity, and temperature gradients. While the single-Maxwellian model successfully describes much of the $\mathbf{v} \cdot \nabla f_e$ term's velocity-space structure, it is unable to properly account for the self-consistent structures in $(\mathbf{F}/m_e) \cdot \nabla f_e$ needed to explain the MMS observations shown here and to satisfy the Vlasov equation in each of those gradient cases.

The previous single-Maxwellian model is successful in accounting for $(\mathbf{F}/m_e) \cdot \nabla f_e$ only in the simplest case where there is a spatial gradient in the density ($\nabla n_e \neq 0$), but no gradients in bulk velocity or temperature ($\nabla U_e = 0$ and $\nabla T_e = 0$). In this case, the bipolar velocity-space signature along the $v_{\perp 12}$ direction associated with $\mathbf{v} \cdot \nabla f_e \approx v_{\perp 12} \nabla_{\perp 12} f_e$ is balanced by terms proportional to $E_{\perp 12} (\partial f_e / \partial v_{\perp 12})$ and $B (\partial f_e / \partial v_{\perp 12})$ (see Equation 2 of Shuster, Gershman, et al. (2021)). However, in the more complicated gradient cases, a single Maxwellian population

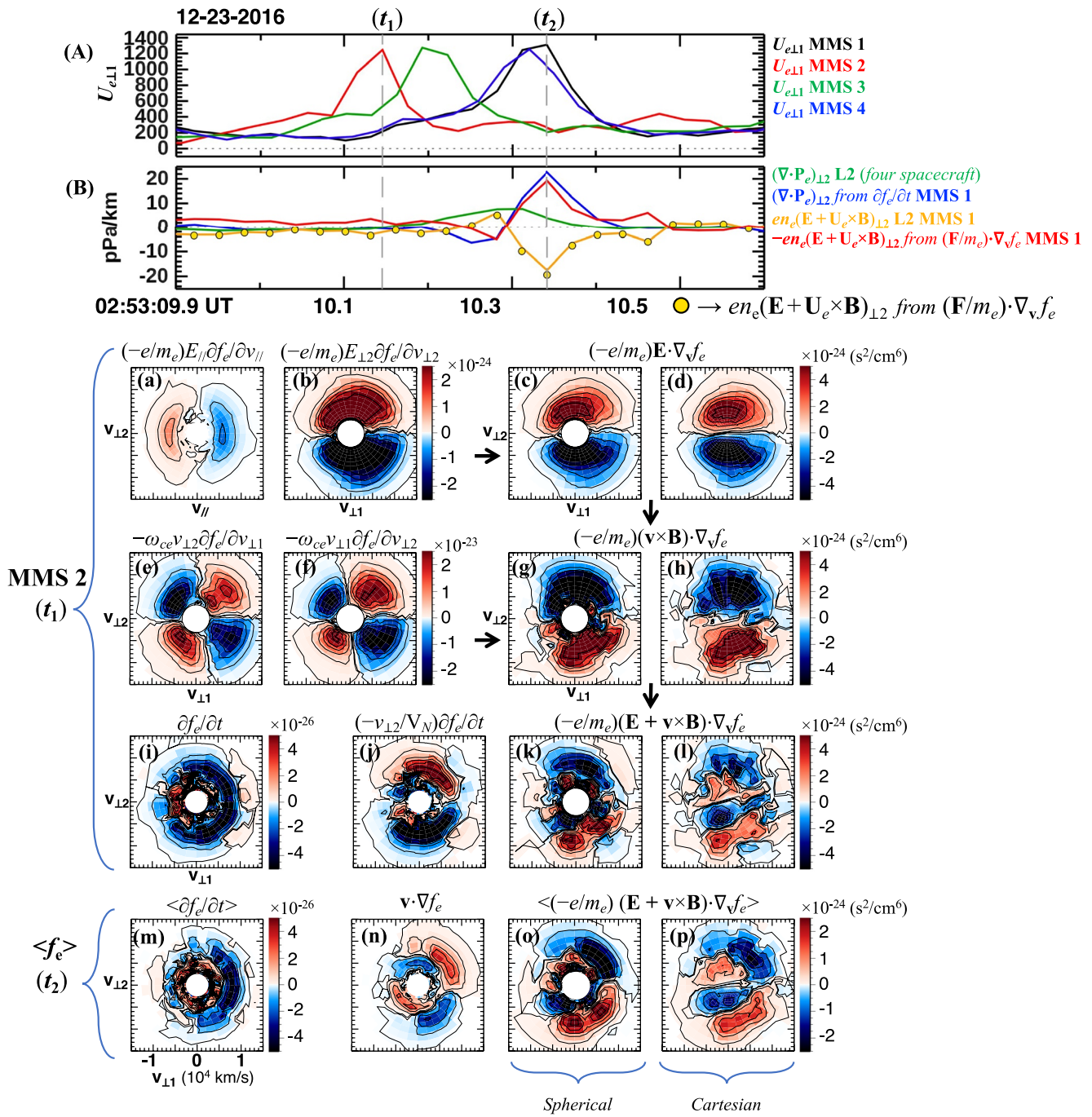


Figure 4.

cannot effect more complicated structure in velocity space other than a bipolar signature; skewed, multicomponent quadrupolar, and ring-like velocity-space structures require the distribution to deviate from a simple Maxwellian.

Extending the model of Shuster, Gershman, et al. (2021), here we model the necessary non-Maxwellianity by representing the distribution as a sum of two spatially varying Maxwellian populations:

$$f_{e1} = n_{e1} \left(\frac{m_e}{2\pi T_{e1}} \right)^{3/2} \exp \left[\frac{-m_e}{2T_{e1}} (\mathbf{v} - \mathbf{U}_{e1})^2 \right] \quad (12)$$

$$f_{e2} = n_{e2} \left(\frac{m_e}{2\pi T_{e2}} \right)^{3/2} \exp \left[\frac{-m_e}{2T_{e2}} (\mathbf{v} - \mathbf{U}_{e2})^2 \right] \quad (13)$$

$$f_e = \left(\frac{1 - \tanh(x/d)}{2} \right) f_{e1} + \left(\frac{1 + \tanh(x/d)}{2} \right) f_{e2}, \quad (14)$$

where each parameter set $\{n_{e1}, \mathbf{U}_{e1}, T_{e1}\}$ and $\{n_{e2}, \mathbf{U}_{e2}, T_{e2}\}$ corresponds to the plasma parameters (density, bulk velocity, and temperature) from each side of the current sheet (denoted by the subscripts “1” and “2”) of the current layer, and the parameter d specifies the gradient scale length. The $\tanh(x/d)$ dependences are used to smoothly transition the distribution from f_{e1} to f_{e2} across the layer. We focus on the distribution at the center of the layer where $x = 0$ so that $f_e = (f_{e1} + f_{e2})/2$ represents a mixture of both populations. Figures 6a and 6b show two schematics illustrating the basic effect of the electric and magnetic fields on the electron distribution (discussed below), and the remaining panels present model results for four gradient situations of interest. The four spatial gradient cases considered are density ∇n_e , bulk velocity $\nabla \mathbf{U}_e$, temperature ∇T_e , and a combination of each of these. The model results for each of these gradient cases correspond to panels (c–e), (f–h), (i–k), and (l–p), respectively.

The simplest density gradient case is understood directly from the schematic diagrams in Figures 6a and 6b, and is illustrated by the first row of Figures 6c–6e. The electric field component $E_{\perp 2}$ directly accelerates electrons in the $-\mathbf{v}_{\perp 2}$ direction (Figure 6a). Thus, electrons with $v_{\perp 2} < 0$ gain energy from the electric field ($\mathbf{J}_e \cdot \mathbf{E} > 0$), while electrons with $v_{\perp 2} > 0$ lose energy ($\mathbf{J}_e \cdot \mathbf{E} < 0$). For half of the velocity-space with $v_{\perp 2} > 0$, these electrons are transported toward regions of locally *increasing* phase space density, hence the quantity $(-e/m_e)E_{\perp 2}\partial f_e/\partial v_{\perp 2} > 0$ (red color). For the other half of the velocity-space with $v_{\perp 2} < 0$, the situation is reversed: these electrons are moved toward regions of *decreasing* phase space density, hence the quantity $(-e/m_e)E_{\perp 2}\partial f_e/\partial v_{\perp 2} < 0$ (blue color). Even though electrons moving through a magnetic field experience a more complicated rotational force, the effect of the magnetic field term $(-e/m_e)(\mathbf{v} \times \mathbf{B}) \cdot \nabla_{\mathbf{v}} f_e$ on a Maxwellian distribution resembles that of the electric field term, as illustrated by the schematic in Figure 6b. Because the term $(-e/m_e)(\mathbf{v} \times \mathbf{B}) \cdot \nabla_{\mathbf{v}} f_e$ is directly proportional to the gyrophase derivative of f_e (see Equation 10), a gyrotropic Maxwellian distribution centered at $U_{e\perp} = 0$ would remain unchanged in the presence of a magnetic field: individual electrons would gyrate in response to \mathbf{B} , but the gyrotropic symmetry of the electron ensemble is preserved. When $U_{e\perp} \neq 0$, as shown in Figure 6b, the gyrophase derivative detects a nonzero signal. For $U_{e\perp 1} > 0$, the gyrophase derivative (taken along a path following the magenta arrow) in the lower half of velocity space with $v_{\perp 2} < 0$ is positive $\partial f_e/\partial \phi_g > 0$ as the magnetic force pushes electrons toward regions of *higher* phase space density (red color). For the other half of velocity space with $v_{\perp 2} > 0$, the gyrophase derivative is negative $\partial f_e/\partial \phi_g < 0$ as the magnetic force moves electrons toward regions of *lower* phase space density (blue color). For the more complicated gradient cases where the distribution is represented by two Maxwellians, each Maxwellian is associated with its own bipolar structure in velocity space due to the net \mathbf{E} and \mathbf{B} forces. The addition of these multiple, overlapping bipolar structures of opposite polarity is capable of producing the ring and skewed quadrupolar structures in $(\mathbf{F}/m_e) \cdot \nabla_{\mathbf{v}} f_e$ necessary to balance $\mathbf{v} \cdot \nabla_{\mathbf{v}} f_e$ in the bulk velocity and temperature gradient cases.

Figures 6c, 6f, 6i, and 6l show the two constituent distributions f_{e1} (orange) and f_{e2} (green) contributing to the total f_e (black) (to avoid crowding these diagrams, the black trace shows $2f_e = f_{e1} + f_{e2}$). The next two panels in each row show the resulting $\mathbf{v} \cdot \nabla_{\mathbf{v}} f_e$ and $(\mathbf{F}/m_e) \cdot \nabla_{\mathbf{v}} f_e$ for the total distribution f_e . We employ the technique of

Figure 4. Magnetospheric Multiscale (MMS) measurements of all intermediary terms needed to compute the full velocity-space gradient term $(\mathbf{F}/m_e) \cdot \nabla_{\mathbf{v}} f_e$, along with comparisons to single-spacecraft and multi-spacecraft measurements of the remaining terms in the Vlasov equation. (a) Four spacecraft measurements of the electron bulk velocity $\mathbf{U}_{e\perp 1}$. (b) Balance of terms in the electron momentum equation: the electron pressure divergence component $(\nabla \cdot \mathbf{P}_e)_{\perp 2}$ computed from the four spacecraft Level 2 (L2) moments (green), $(\nabla \cdot \mathbf{P}_e)_{\perp 2}$ inferred from MMS 1 measurements of $\partial f_e/\partial t$ (blue), the force density $en_e(\mathbf{E} + \mathbf{U}_e \times \mathbf{B})$ computed from the standard L2 moments (orange), and $-en_e(\mathbf{E} + \mathbf{U}_e \times \mathbf{B})$ computed from taking the first moment of $(\mathbf{F}/m_e) \cdot \nabla_{\mathbf{v}} f_e$ (red) for comparison with $(\nabla \cdot \mathbf{P}_e)_{\perp 2}$. The gold circles benchmark our moments computation, showing how the integral quantity $\int v_{\perp 2}(\mathbf{F} \cdot \nabla_{\mathbf{v}} f_e)d^3v$ aligns closely with the standard measure of the force density term $en_e(\mathbf{E} + \mathbf{U}_e \times \mathbf{B})_{\perp 2}$. The panels in (c), (g), (k), and (o) show quantities computed in spherical velocity-space coordinates native to the FPI instrumentation, while panels (d), (h), (l), and (p) are computed after interpolating f_e to a Cartesian velocity-space grid. (a) $(-e/m_e)E_{\parallel 1}\partial f_e/\partial v_{\parallel 1}$ and (b) $(-e/m_e)E_{\perp 2}\partial f_e/\partial v_{\perp 2}$ provide the dominant contributions to the full electric field term (c, d) $(-e/m_e)\mathbf{E} \cdot \nabla_{\mathbf{v}} f_e$. (e) $-\omega_{ce}v_{\perp 2}\partial f_e/\partial v_{\perp 1}$ and (f) $-\omega_{ce}v_{\perp 1}\partial f_e/\partial v_{\perp 2}$ are subtracted to obtain the full gyrophase derivative term (g, h) $(-e/m_e)(\mathbf{v} \times \mathbf{B}) \cdot \nabla_{\mathbf{v}} f_e = \omega_{ce}\partial f_e/\partial \phi_g$. Panels (i)–(l) show all three terms of the electron Vlasov equation observed by MMS 2: (i) $\partial f_e/\partial t$, (j) $(-v_{\perp 2}/V_N)\partial f_e/\partial t$ as a higher resolution proxy for $\mathbf{v} \cdot \nabla_{\mathbf{v}} f_e$, and (k, l) the full velocity-space gradient term $(\mathbf{F}/m_e) \cdot \nabla_{\mathbf{v}} f_e$ computed by adding (c, d) $(-e/m_e)\mathbf{E} \cdot \nabla_{\mathbf{v}} f_e$ and (g, h) $(-e/m_e)(\mathbf{v} \times \mathbf{B}) \cdot \nabla_{\mathbf{v}} f_e$ together. Panels (m)–(p) show the three Vlasov equation terms at time t_2 : (m) four-spacecraft average $\langle \partial f_e/\partial t \rangle$, (n) four-spacecraft measurement of $\mathbf{v} \cdot \nabla_{\mathbf{v}} f_e$, (o, p) four-spacecraft average $\langle (\mathbf{F}/m_e) \cdot \nabla_{\mathbf{v}} f_e \rangle$. The orientation of all the velocity-space slices is $v_{\perp 1}$ (horizontal) versus $v_{\perp 2}$ (vertical) except for panel (a) which is $v_{\parallel 1}$ (horizontal) versus $v_{\perp 1}$ (vertical).

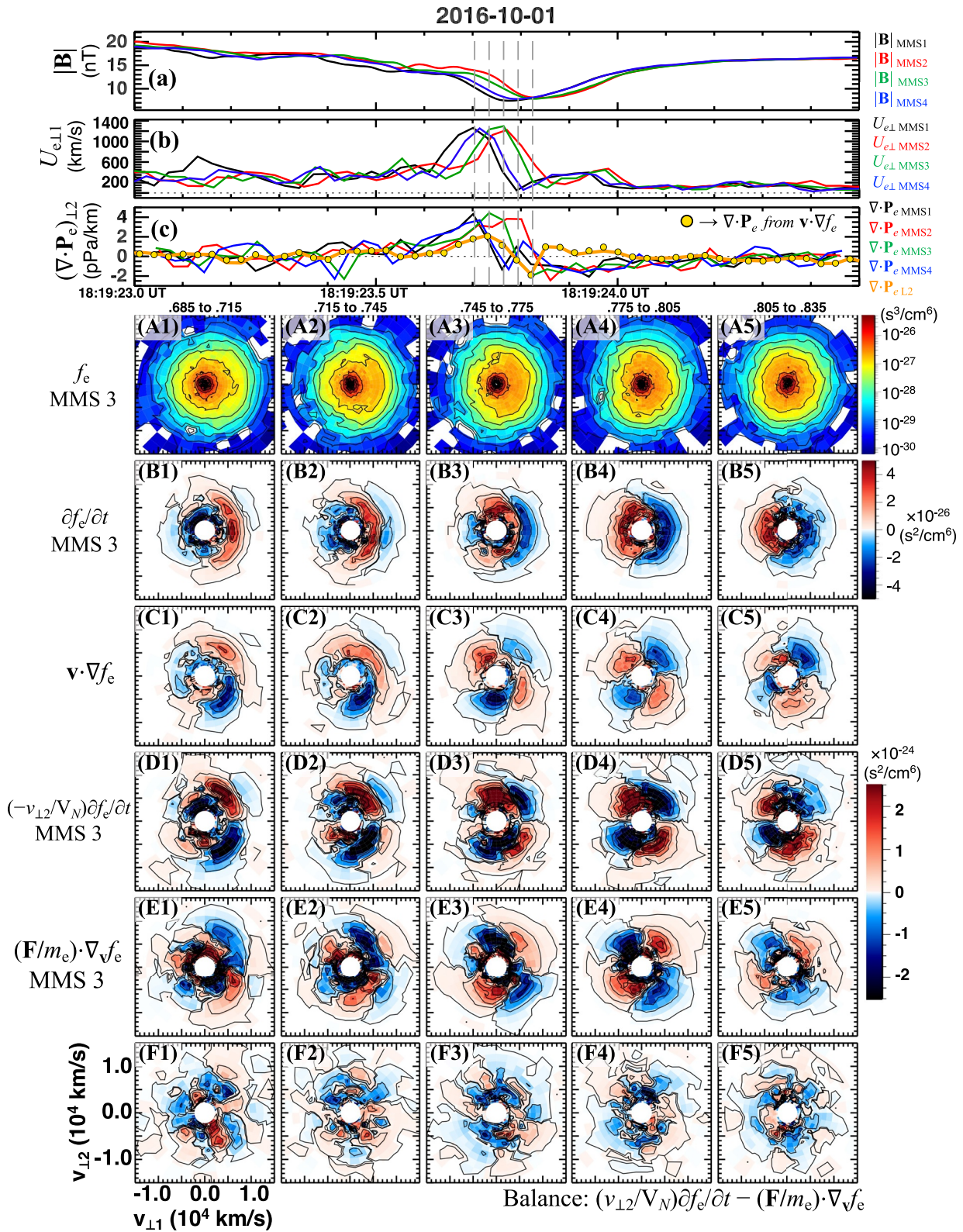


Figure 5.

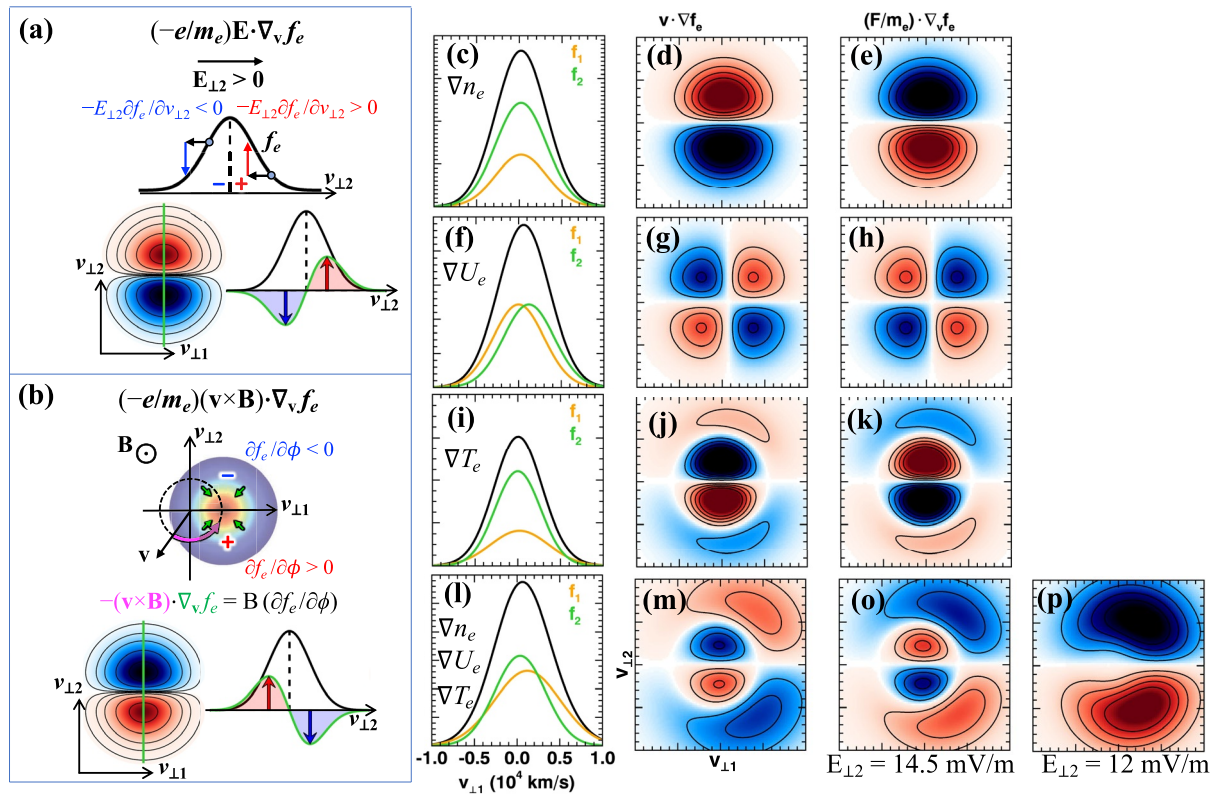


Figure 6. Double-Maxwellian model results and schematics offering an intuition for interpreting how the balance between the $\mathbf{v} \cdot \nabla f_e$ and $(\mathbf{F}/m_e) \cdot \nabla f_e$ terms is achieved in the electron Vlasov equation for a variety of gradient contexts arising at Earth's magnetopause. (a, b) Schematics illustrating the effect of the (a) electric and (b) magnetic forces on the velocity-space structure of the electron distribution when f_e is assumed to be a single Maxwellian. Panels (c, d, e), (f, g, h), (i, j, k), and (l, m, o, p) feature results applicable to a spatial gradient in the electron density ∇n_e , bulk velocity ∇U_e , temperature ∇T_e , and a combination of these gradients, respectively. The column of panels (c, f, i, l) show the two Maxwellian populations f_{e1} (orange) and f_{e2} (green) whose sum is equal to the total electron distribution $f_e = (f_{e1} + f_{e2})/2$ (black traces show $2f_e$ to avoid crowding the f_{e1} and f_{e2} curves). The panels in column (d, g, j, m) show $\mathbf{v} \cdot \nabla f_e$, while (e, h, k, o) show $(\mathbf{F}/m_e) \cdot \nabla f_e$. Panel (p) shows the sensitivity of the total f_e distribution to the fields quantities: the correct electric field $E_{12} = 14.5$ mV/m yields a $(\mathbf{F}/m_e) \cdot \nabla f_e$ structure which balances $\mathbf{v} \cdot \nabla f_e$ in panel (m); however, when the electric field is artificially adjusted by a few mV/m to $E_{12} = 12$ mV/m, the needed quadrupole structure vanishes as the inner bipolar peaks associated with f_{e2} are significantly reduced.

Shuster, Gershman, et al. (2021) to evaluate the total term $\mathbf{v} \cdot \nabla f_e = (\mathbf{v} \cdot \nabla f_{e1} + \mathbf{v} \cdot \nabla f_{e2})/2$, and we use the model defined above in Equations 12–14 to directly evaluate $(\mathbf{F}/m_e) \cdot \nabla f_e = [(\mathbf{F}/m_e) \cdot \nabla f_{e1} + (\mathbf{F}/m_e) \cdot \nabla f_{e2}]/2$. Because the total distribution f_e is a sum of two Maxwellians, the total $\mathbf{v} \cdot \nabla f_e$ structures look very similar to the results presented in Shuster, Gershman, et al. (2021) (see their fig. 1). However, here, the inherent non-Maxwellianity of the combined model distribution defined by $f_e = (f_{e1} + f_{e2})/2$ introduces sufficient complexity to the shape of f_e so that the velocity-space gradient term $(\mathbf{F}/m_e) \cdot \nabla f_e$ develops to self-consistently balance the spatial gradient term in each gradient situation. We note that neither the single-Maxwellian nor the double-Maxwellian models satisfy the Vlasov equation exactly (for a recent treatment of an exact solution to the Vlasov-Maxwell system, see e.g., Shuster, Bessho, et al. (2021)). Nevertheless, these analytical models are suggested for intuitive purposes without having to carry out the sophisticated solution techniques required for the Vlasov-Maxwell system, and there is excellent qualitative agreement between the spatial and velocity-space gradient terms as is evident by comparing the $\mathbf{v} \cdot \nabla f_e$ and $(\mathbf{F}/m_e) \cdot \nabla f_e$ columns (compare panels d, g, j, m to e, h, k, o, respectively) of Figure 6.

Figure 5. Spatiotemporal evolution of the velocity-space balance of each term of the electron Vlasov equation for the event observed by MMS on 1 October 2016. (a)–(c) Four-spacecraft measurements of plasma quantities of interest for context: (a) Total magnetic field strength $|\mathbf{B}|$, (b) perpendicular electron bulk velocity $U_{e\perp 1}$, and (c) single-spacecraft and multi-spacecraft measurements of \perp_2 -component of the electron pressure tensor $(\nabla \cdot \mathbf{P}_e)_{\perp 2}$ (analogous to Figure 2c), with five dashed lines indicating the times at which the $v_{\perp 1}$ – $v_{\perp 2}$ distribution slices below are taken. Rows A–F show single-spacecraft measurements from MMS 3, while Row C shows measurements computed from the four spacecraft. (A1–A5) Electron phase space density f_e showing the various nongyrotropic and elongated velocity-space structures which develop within the current layer. (B1–B5) $\partial f_e / \partial t$ from MMS 3. (C1–C5) four-spacecraft spatial gradient term $\mathbf{v} \cdot \nabla f_e$. (D1–D5) $(-v_{\perp 2}/V_N) \partial f_e / \partial t$ from MMS 3, representing a higher resolution, single-spacecraft proxy for $\mathbf{v} \cdot \nabla f_e$. (E1–E5) $(\mathbf{F}/m_e) \cdot \nabla f_e$. (F1–F5) Difference between $(v_{\perp 2}/V_N) \partial f_e / \partial t$ and $(\mathbf{F}/m_e) \cdot \nabla f_e$, giving a qualitative indication of how the velocity-space balance is achieved for the electron Vlasov equation terms.

Figure 6p shows the sensitivity of the velocity-space structures in $(\mathbf{F}/m_e) \cdot \nabla_{\mathbf{v}} f_e$ to the magnitude of the measured fields quantities: adjusting the electric field by only 2 or 3 mV/m removes the inner bipolar structure needed to balance the $\mathbf{v} \cdot \nabla f_e$.

4. Conclusions, Discussion, and Outlook

We computed and compared the velocity-space structure of all three terms in the electron Vlasov equation using MMS measurements of electron-scale current layers observed in the vicinity of Earth's magnetopause. In particular, we presented MMS measurements of the velocity-space gradient term $(\mathbf{F}/m_e) \cdot \nabla_{\mathbf{v}} f_e$ and each of the terms needed to compute it, including $(-e/m_e)E_{\parallel} \partial f_e / \partial v_{\parallel}$, which is specifically relevant to recent studies quantifying the non-resonant FPC associated with direct energization by the parallel electric field (Klein & Howes, 2016; McCubbin et al., 2022). Using our methodology, we discussed the physical effect that the electric and magnetic fields have on the electron ensemble via $(-e/m_e)\mathbf{E} \cdot \nabla_{\mathbf{v}} f_e$ and $(-e/m_e)(\mathbf{v} \times \mathbf{B}) \cdot \nabla_{\mathbf{v}} f_e$, and how these terms cooperate to balance the previously reported spatial gradient structures for a variety of spatial gradient contexts observed by MMS in the vicinity of the magnetopause (Shuster, Gershman, et al., 2021). In the same way that the velocity-space integral of the quantity $\mathbf{v}(\mathbf{v} \cdot \nabla f_e)$ is directly related to $\nabla \cdot \mathbf{P}_e$ as discussed by Shuster et al. (2019), we note that the integral of the quantity $(1/2)m_e v^2 (\mathbf{F}/m_e) \cdot \nabla_{\mathbf{v}} f_e$ is the velocity-space analog of the electron energy conversion term $\mathbf{J}_e \cdot \mathbf{E}$. The regions of alternating polarity in the velocity-space structure of $(\mathbf{F}/m_e) \cdot \nabla_{\mathbf{v}} f_e$ highlight the relevant energies and directions of the electrons that are most efficiently accelerated (or decelerated) by the electric and magnetic fields, with the net result being the total amount of energy that is transferred between the electric field and the electron ensemble as measured by $\mathbf{J}_e \cdot \mathbf{E}$.

We implemented fourth-order finite difference estimates for the temporal and velocity-space derivatives to improve the accuracy of the resulting FPI gradient measurements. In particular, we found that for approximately steady-state structures moving past MMS on the order of 50–100 km/s, the temporal derivative $\partial f_e / \partial t$ can be used to construct a single-spacecraft version of the spatial derivative ∇f_e . This is especially useful for computing higher resolution single-spacecraft measurements of quantities such as the electron pressure divergence $\nabla \cdot \mathbf{P}_e$ within electron-scale structures smaller than the spacecraft separation, which is commonly the case for thin current sheets and EDRs at the magnetopause. Using these single-spacecraft measurements, we found that the perpendicular contribution to $\nabla \cdot \mathbf{P}_e$ was three to four times larger than previously reported (Shuster et al., 2019), which affects our understanding of the force balance of terms in the electron momentum equation and generalized Ohm's law (e.g., Beedle et al., 2022). Additionally, we showed single-spacecraft measurements of $(\nabla \cdot \mathbf{P}_e)_{\parallel}$ that exhibit better agreement with the extended regions of enhanced parallel electric field E_{\parallel} similar to the EDR event first reported by Wilder et al. (2017) within the magnetosheath, and consistent with 3D particle-in-cell (PIC) simulations (Liu et al., 2013). Our approach enables identification of the particular velocity-space structures of the relevant Vlasov equation terms that contribute directly to $(\nabla \cdot \mathbf{P}_e)_{\parallel}$ and thus support the extended regions of nonideal E_{\parallel} . Although here we focused on terms of the electron Vlasov equation within electron-scale current layers at the dayside magnetopause in the present study, we note that this approach is also applicable to larger-scale structures in other environments as well. For example, MMS dual ion spectrometer measurements may be utilized to analyze terms of the ion Vlasov equation applicable to ion-scale current sheets such as those commonly found in the Earth's magnetotail. Furthermore, this method of estimating gradient quantities such as the electron pressure divergence and other terms appearing in the generalized Ohm's law from a single spacecraft is especially useful for events when four spacecraft data are not readily available, such as when data are missing from one spacecraft, or when the four spacecraft are not flying in a tetrahedral formation.

Similar to how Shuster, Gershman, et al. (2021) developed a simplified, single Maxwellian model for $\mathbf{v} \cdot \nabla f_e$, here we introduce an additional layer of sophistication to that approach by representing the electron distribution at the center of the current layer as a sum of two Maxwellians: $f_e = (f_{e1} + f_{e2})/2$, where f_{e1} and f_{e2} are determined from observations of the plasma moments on either side of the layer. We show that for this double-Maxwellian model distribution, ∇f_e retains a similar structure to the results of Shuster, Gershman, et al. (2021), but the non-Maxwellian nature of the combined distribution permits a nontrivial signal in the $(\mathbf{F}/m_e) \cdot \nabla_{\mathbf{v}} f_e$ term that closely resembles the $\mathbf{v} \cdot \nabla f_e$ structures. While our double-Maxwellian model does not satisfy the Vlasov equation exactly, the improvement is reminiscent of the recent work by Allanson et al. (2017) reporting an exact Vlasov-Maxwell equilibrium solution for an asymmetric current layer that consists of a sum of four drifting

Maxwellian populations, a form of the distribution function that is amenable to recent multi-beam analysis methods developed by Goldman et al. (2021).

Due to the limitations of the MMS temporal, spatial, and velocity-space resolutions, we note that the Vlasov equation terms we computed (e.g., row F in Figure 5) do not sum to zero exactly throughout velocity-space. Because the magnetopause environment is believed to be collisionless to an excellent approximation, we do not believe this deviation from zero to be physical; rather, we suspect the instrumentation on MMS, while groundbreaking, was not specifically designed to measure the entire velocity space with the exactness that satisfying the Vlasov equation would require, consistent with Argall et al. (2022). Nevertheless, we emphasize the remarkable qualitative and visual agreement between $\mathbf{v} \cdot \nabla f_e$ and $(\mathbf{F}/m_e) \cdot \nabla_{\mathbf{v}} f_e$ (i.e., comparing rows D and E in Figure 5) that MMS successfully captures. This consistency agrees with expectation based on the Vlasov equation, and serves as testament to the unprecedented FPI and fields instrumentation onboard the MMS tetrahedron, which clearly have surpassed their original design requirements. Furthermore, these results have important implications applicable whenever we believe MMS is sampling regions of collisionless plasma, that is, whenever we believe the Vlasov equation is satisfied: from careful measurements of two of the terms in the Vlasov equation, in principle, we may obtain the third without needing to measure it. This application is especially useful for single spacecraft missions where multiple spatial points cannot be simultaneously measured, and for multi-spacecraft missions such as MMS where, by having access to all three terms, we are able to choose the term with optimal resolution for studying the particular plasma phenomenon of interest.

The ability to measure each term of the Vlasov equation has implications for assessing the degree to which plasmas are actually “collisionless,” for example, in the weakly collisional solar wind, or in the meso-scale transition region between the outer and inner magnetosphere regions (i.e., going from the collisionless magnetotail region to the collisional ionosphere). Quantifying the collisionality of plasmas is immediately relevant to the outstanding mystery of how dissipative processes, like magnetic reconnection, are able to occur in the collisionless regime. The presence of collisions, if detected, and even if present for a portion of the plasma's velocity space, could serve as a source of the resistivity needed to drive or initiate the reconnection energy conversion process. This work, with the help of state-of-the-art kinetic plasma simulations, such as PIC simulations, may serve as a guide for future mission concepts and instrument designs specifically targeting kinetic processes described by the ion and electron Vlasov equations.

Appendix A: Computing Velocity-Space Gradients With FPI

Since the FPI energies follow an approximately logarithmic spacing, we utilize the following coordinate transformation:

$$E' = E_0 \ln(E/E_0), \quad (\text{A1})$$

where E (in eV) specifies the FPI energy targets, and E_0 is taken to be 1 eV for unit consistency. With this substitution, the spacing between consecutive E' targets is approximately a constant: $\Delta E'$. Starting from the original phase space density measurements in FPI coordinates $f_e = f_e(E, \theta, \phi)$, and noting that E is independent of both θ and ϕ , we therefore obtain $\partial f_e / \partial E$ as follows:

$$\frac{\partial f_e}{\partial E} = \frac{\partial f_e}{\partial E'} \frac{dE'}{dE} = \frac{E_0}{E} \frac{\partial f_e}{\partial E'}, \quad (\text{A2})$$

where we approximate $\partial f_e / \partial E'$ at E'_i for all $\{\theta, \phi\}$ using a fourth order centered difference estimation, given by:

$$\frac{\partial f_e}{\partial E'} \approx \frac{-f_e(E'_{i+2}) + 8f_e(E'_{i+1}) - 8f_e(E'_{i-1}) + f_e(E'_{i-2})}{12\Delta E'}. \quad (\text{A3})$$

Similarly, we estimate $\partial f_e / \partial \theta$ at θ_i for all $\{E, \phi\}$ and $\partial f_e / \partial \phi$ at ϕ_i for all $\{E, \theta\}$ via the following.

$$\frac{\partial f_e}{\partial \theta} \approx \frac{-f_e(\theta_{i+2}) + 8f_e(\theta_{i+1}) - 8f_e(\theta_{i-1}) + f_e(\theta_{i-2})}{12\Delta \theta} \quad (\text{A4})$$

$$\frac{\partial f_e}{\partial \phi} \approx \frac{-f_e(\phi_{i+2}) + 8f_e(\phi_{i+1}) - 8f_e(\phi_{i-1}) + f_e(\phi_{i-2})}{12\Delta \phi}, \quad (\text{A5})$$

where $\Delta\theta = \Delta\phi = 11.25^\circ$. To compute $\partial f_e / \partial E'$ at the energy endpoints, we use fourth order forward and backward difference estimations. We evaluate $\partial f_e / \partial \phi$ at the ϕ endpoints by utilizing the periodicity of the azimuthal ϕ grid. Since the polar θ grid is not periodic, we note that some terms appearing in the evaluation of $\partial f_e / \partial \theta$ at the θ endpoint locations θ_0 , θ_1 , θ_{14} , and θ_{15} require the ϕ coordinate to be flipped by 180° . To convert the energy space derivatives to derivatives in velocity space, we use the non-relativistic transformation $v = \sqrt{2E/m_e}$ along with Equation A2, from which we readily obtain:

$$\frac{df_e}{dv} = \frac{\partial f_e}{\partial E} \frac{dE}{dv} = m_e v \frac{\partial f_e}{\partial E} = m_e v \frac{E_0}{E} \frac{\partial f_e}{\partial E'} = E_0 \sqrt{\frac{2m_e}{E}} \frac{\partial f_e}{\partial E'}. \quad (\text{A6})$$

Ultimately, we wish to obtain derivatives with respect to Cartesian velocity space coordinates in order to directly evaluate the term $(\mathbf{F}/m_e) \cdot \nabla_{\mathbf{v}} f_e$. Converting from spherical velocity space coordinates (v, θ, ϕ) to Cartesian velocity space coordinates (v_x, v_y, v_z) via the coordinate relationships.

$$v^2 = v_x^2 + v_y^2 + v_z^2 \quad (\text{A7})$$

$$v_x = v \sin(\theta) \cos(\phi) \quad (\text{A8})$$

$$v_y = v \sin(\theta) \sin(\phi) \quad (\text{A9})$$

$$v_z = v \cos(\theta) \quad (\text{A10})$$

$$v_y/v_x = \tan(\phi), \quad (\text{A11})$$

we construct the Cartesian velocity space derivatives as follows:

$$\frac{\partial f_e}{\partial v_x} = \frac{\partial f_e}{\partial v} \frac{\partial v}{\partial v_x} + \frac{\partial f_e}{\partial \theta} \frac{\partial \theta}{\partial v_x} + \frac{\partial f_e}{\partial \phi} \frac{\partial \phi}{\partial v_x} \quad (\text{A12})$$

$$\frac{\partial f_e}{\partial v_y} = \frac{\partial f_e}{\partial v} \frac{\partial v}{\partial v_y} + \frac{\partial f_e}{\partial \theta} \frac{\partial \theta}{\partial v_y} + \frac{\partial f_e}{\partial \phi} \frac{\partial \phi}{\partial v_y} \quad (\text{A13})$$

$$\frac{\partial f_e}{\partial v_z} = \frac{\partial f_e}{\partial v} \frac{\partial v}{\partial v_z} + \frac{\partial f_e}{\partial \theta} \frac{\partial \theta}{\partial v_z} + \frac{\partial f_e}{\partial \phi} \frac{\partial \phi}{\partial v_z}, \quad (\text{A14})$$

which can be written in matrix form as:

$$\begin{bmatrix} \frac{\partial v}{\partial v_x} & \frac{\partial \theta}{\partial v_x} & \frac{\partial \phi}{\partial v_x} \\ \frac{\partial v}{\partial v_y} & \frac{\partial \theta}{\partial v_y} & \frac{\partial \phi}{\partial v_y} \\ \frac{\partial v}{\partial v_z} & \frac{\partial \theta}{\partial v_z} & \frac{\partial \phi}{\partial v_z} \end{bmatrix} \cdot \begin{bmatrix} \frac{\partial f_e}{\partial v} \\ \frac{\partial f_e}{\partial \theta} \\ \frac{\partial f_e}{\partial \phi} \end{bmatrix} = \begin{bmatrix} \frac{\partial f_e}{\partial v_x} \\ \frac{\partial f_e}{\partial v_y} \\ \frac{\partial f_e}{\partial v_z} \end{bmatrix} \quad (\text{A15})$$

Evaluating each of the nine coordinate derivatives explicitly, we have:

$$\frac{\partial v}{\partial v_x} = \sin(\theta) \cos(\phi) \quad (\text{A16})$$

$$\frac{\partial v}{\partial v_y} = \sin(\theta) \sin(\phi) \quad (\text{A17})$$

$$\frac{\partial v}{\partial v_z} = \cos(\theta) \quad (\text{A18})$$

$$\frac{\partial \theta}{\partial v_x} = \frac{\cos(\theta) \cos(\phi)}{v} \quad (\text{A19})$$

$$\frac{\partial \theta}{\partial v_y} = \frac{\cos(\theta) \sin(\phi)}{v} \quad (\text{A20})$$

$$\frac{\partial \theta}{\partial v_z} = \frac{-\sin(\theta)}{v} \quad (\text{A21})$$

$$\frac{\partial \phi}{\partial v_x} = \frac{-\sin(\phi) \cos(\phi)}{v_x} = \frac{-\sin(\phi)}{v \sin(\theta)} \quad (\text{A22})$$

$$\frac{\partial \phi}{\partial v_y} = \frac{\cos^2(\phi)}{v_x} = \frac{\cos(\phi)}{v \sin(\theta)} \quad (\text{A23})$$

$$\frac{\partial \phi}{\partial v_z} = 0 \quad (\text{A24})$$

Substituting Equations A6 and A16 to A24 into Equation A15, we obtain the desired Cartesian velocity-space derivative skymaps $\partial f_e / \partial v_x$, $\partial f_e / \partial v_y$, and $\partial f_e / \partial v_z$ as functions of the original FPI energy space coordinates $\{E, \theta, \phi\}$.

The rightmost column of Figure 4 presents results obtained from implementing an alternative computation approach that involves first interpolating $f_e(E, \theta, \phi)$ to a Cartesian velocity space grid: $f_e(v_x, v_y, v_z)$. In these Cartesian coordinates, the desired derivatives are readily obtained via fourth order finite difference estimations as follows.

$$\frac{\partial f_e}{\partial v_x} \approx \frac{-f_e(v_x^{i+2}) + 8f_e(v_x^{i+1}) - 8f_e(v_x^{i-1}) + f_e(v_x^{i-2})}{12\Delta v_x} \quad (\text{A25})$$

$$\frac{\partial f_e}{\partial v_y} \approx \frac{-f_e(v_y^{j+2}) + 8f_e(v_y^{j+1}) - 8f_e(v_y^{j-1}) + f_e(v_y^{j-2})}{12\Delta v_y} \quad (\text{A26})$$

$$\frac{\partial f_e}{\partial v_z} \approx \frac{-f_e(v_z^{k+2}) + 8f_e(v_z^{k+1}) - 8f_e(v_z^{k-1}) + f_e(v_z^{k-2})}{12\Delta v_z} \quad (\text{A27})$$

Here, we note that assuming f_e approaches 0 sufficiently fast as $|v| \rightarrow \infty$, taking the first moment of the electron Vlasov equation (i.e., multiplying Equation 1 by the particle momentum $m_e \mathbf{v}$ and integrating over velocity space) yields the net force density acting on the electron ensemble:

$$\int \mathbf{v}(\mathbf{F} \cdot \nabla_{\mathbf{v}} f_e) d^3 v = en_e(\mathbf{E} + \mathbf{U}_e \times \mathbf{B}), \quad (\text{A28})$$

where $\mathbf{F} = -(e/m_e)(\mathbf{E} + \mathbf{v} \times \mathbf{B})$ for an electron. Analogously to how the spatial gradient term ∇f_e is fundamentally related to $\nabla \cdot \mathbf{P}_e$ as discussed by Shuster et al. (2019), the velocity-space gradient term $\nabla_{\mathbf{v}} f_e$ is the kinetic origin of the electron energy conversion term $\mathbf{J}_e \cdot \mathbf{E}$ as illustrated by the following integral equation for the second moment:

$$\frac{1}{2} m_e \int v^2 (\mathbf{F}/m_e) \cdot \nabla_{\mathbf{v}} f_e d^3 v = en_e \mathbf{U}_e \cdot \mathbf{E} = -\mathbf{J}_e \cdot \mathbf{E}, \quad (\text{A29})$$

where $\mathbf{J}_e = -en_e \mathbf{U}_e$ is the electron contribution to the current (e.g., Gurnett & Bhattacharjee, 2005). Thus, velocity-space visualizations of $(\mathbf{F}/m_e) \cdot \nabla_{\mathbf{v}} f_e$ provide a kinetic perspective that illuminates which electron populations contribute substantially to $\mathbf{J}_e \cdot \mathbf{E}$.

Acknowledgments

J.R.S. thanks K. Springfield for encouraging discussions throughout the preparation of this work. This research was supported in part by NASA grants to the Fast Plasma Investigation, FIELDS team, and Theory and Modeling program of the MMS mission. J.R.S. was supported by NASA Grants 80NSSC21K0732 and 80NSSC21K1482. R.E.D. was supported by NASA Grant 80NSSC22K1109. T.C.L. was supported by NSF Grant AGS-2000222. J.E.S. is supported by the Royal Society University Research Fellowship URF\R1\201286.

Data Availability Statement

The authors especially thank the MMS instrument teams for providing unprecedented, high-quality data sets, available to the public via <https://lasp.colorado.edu/mms/sdc/public/>.

References

- Afshari, A. S., Howes, G. G., Kletzing, C. A., Hartley, D. P., & Boardsen, S. A. (2021). The importance of electron Landau damping for the dissipation of turbulent energy in terrestrial magnetosheath plasma. *Journal of Geophysical Research: Space Physics*, 126(12), e2021JA029578. <https://doi.org/10.1029/2021JA029578>
- Allanson, O., Wilson, F., Neukirch, T., Liu, Y.-H., & Hodgson, J. D. B. (2017). Exact Vlasov-Maxwell equilibria for asymmetric current sheets. *Geophysical Research Letters*, 44(17), 8685–8695. <https://doi.org/10.1002/2017GL074168>

- Argall, M. R., Barbhuiya, M. H., Cassak, P. A., Wang, S., Shuster, J., Liang, H., et al. (2022). Theory, observations, and simulations of kinetic entropy in a magnetotail electron diffusion region. *Physics of Plasmas*, 29(2), 022902. <https://doi.org/10.1063/5.0073248>
- Beedle, J. M. H., Gershman, D. J., Uritsky, V. M., Phan, T. D., & Giles, B. L. (2022). A systematic look at the temperature gradient contribution to the dayside magnetopause current. *Geophysical Research Letters*, 49(4), e2021GL097547. <https://doi.org/10.1029/2021GL097547>
- Bessho, N., Chen, L.-J., & Hesse, M. (2016). Electron distribution functions in the diffusion region of asymmetric magnetic reconnection. *Geophysical Research Letters*, 43(5), 1828–1836. <https://doi.org/10.1002/2016GL067886>
- Bessho, N., Chen, L.-J., Hesse, M., & Wang, S. (2017). The effect of reconnection electric field on crescent and U-shaped distribution functions in asymmetric reconnection with no guide field. *Physics of Plasmas*, 24(7), 072903. <https://doi.org/10.1063/1.4989737>
- Burch, J. L., Torbert, R. B., Phan, T. D., Chen, L.-J., Moore, T. E., Ergun, R. E., et al. (2016). Electron-scale measurements of magnetic reconnection in space. *Science*, 352(6290), aaf2939. <https://doi.org/10.1126/science.aaf2939>
- Chen, C., Klein, K., & Howes, G. (2019). Evidence for electron Landau damping in space plasma turbulence. *Nature Communications*, 10(740), 740. <https://doi.org/10.1038/s41467-019-08435-3>
- Chen, L.-J., Hesse, M., Wang, S., Bessho, N., & Daughton, W. (2016). Electron energization and structure of the diffusion region during asymmetric reconnection. *Geophysical Research Letters*, 43(6), 2405–2412. <https://doi.org/10.1002/2016GL068243>
- Chen, L.-J., Hesse, M., Wang, S., Gershman, D., Ergun, R., Pollock, C., et al. (2016). Electron energization and mixing observed by MMS in the vicinity of an electron diffusion region during magnetopause reconnection. *Geophysical Research Letters*, 43(12), 6036–6043. <https://doi.org/10.1002/2016GL069215>
- Ergun, R. E., Tucker, S., Westfall, J., Goodrich, K. A., Malaspina, D. M., Summers, D., et al. (2016). The axial double probe and fields signal processing for the MMS mission. *Space Science Reviews*, 199(1), 167–188. <https://doi.org/10.1007/s11214-014-0115-x>
- Genestreti, K. J., Varsani, A., Burch, J. L., Cassak, P. A., Torbert, R. B., Nakamura, R., et al. (2018). MMS observation of asymmetric reconnection supported by 3-D electron pressure divergence. *Journal of Geophysical Research: Space Physics*, 123(3), 1806–1821. <https://doi.org/10.1002/2017JA025019>
- Gershman, D. J., Dorelli, J. C., F-Viñas, A., & Pollock, C. J. (2015). The calculation of moment uncertainties from velocity distribution functions with random errors. *Journal of Geophysical Research: Space Physics*, 120(8), 6633–6645. <https://doi.org/10.1002/2014JA020775>
- Gershman, D. J., F-Viñas, A., Dorelli, J. C., Boardsen, S. A., Avano, L. A., Bellan, P. M., et al. (2017). Wave-particle energy exchange directly observed in a kinetic Alfvén-branch wave. *Nature Communications*, 8(1), 14719. <https://doi.org/10.1038/ncomms14719>
- Goldman, M. V., Newman, D. L., Eastwood, J. P., Lapenta, G., Burch, J. L., & Giles, B. (2021). Multi-beam energy moments of measured compound ion velocity distributions. *Physics of Plasmas*, 28(10), 102305. <https://doi.org/10.1063/5.0063431>
- Gurnett, D. A., & Bhattacharjee, A. (2005). *Introduction to plasma physics: With space and laboratory applications*. Cambridge University Press. <https://doi.org/10.1017/CBO9780511809125>
- Gurram, H., Egedal, J., & Daughton, W. (2021). Shear Alfvén waves driven by magnetic reconnection as an energy source for the aurora borealis. *Geophysical Research Letters*, 48(14), e2021GL094201. <https://doi.org/10.1029/2021GL094201>
- Harris, E. G. (1962). On a plasma sheath separating regions of oppositely directed magnetic field. *Nuovo Cimento A*, 23(1), 115–121. <https://doi.org/10.1007/BF02733547>
- Harvey, C. C. (1998). Spatial gradients and the volumetric tensor. In G. Paschmann & P. W. Daly (Eds.), *Analysis methods for multi-spacecraft data*. ISSI Scientific Reports Series. (pp. 307–322).
- Horvath, S. A., Howes, G. G., & McCubbin, A. J. (2020). Electron Landau damping of kinetic Alfvén waves in simulated magnetosheath turbulence. *Physics of Plasmas*, 27(10), 102901. <https://doi.org/10.1063/5.0021727>
- Klein, K. G., & Howes, G. G. (2016). Measuring collisionless damping in heliospheric plasmas using field-particle correlations. *The Astrophysical Journal Letters*, 826(2), L30. <https://doi.org/10.3847/2041-8205/826/2/L30>
- Landau, L. D. (1946). On the vibrations of the electronic plasma. *Journal of Physics (USSR)*, X(1), 25–34. <https://doi.org/10.1016/B978-0-08-010586-4.50066-3>
- Li, T. C., Howes, G., Klein, K., Liu, Y.-H., & TenBarge, J. M. (2019). Collisionless energy transfer in kinetic turbulence: Field-particle correlations in Fourier space. *Journal of Plasma Physics*, 85(4), 905850406. <https://doi.org/10.1017/S0022377819000515>
- Lindqvist, P.-A., Olsson, G., Torbert, R. B., King, B., Granoff, M., Rau, D., et al. (2016). The spin-plane double probe electric field instrument for MMS. *Space Science Reviews*, 199(1), 137–165. <https://doi.org/10.1007/s11214-014-0116-9>
- Liu, Y.-H., Daughton, W., Karimabadi, H., Li, H., & Roytershteyn, V. (2013). Bifurcated structure of the electron diffusion region in three-dimensional magnetic reconnection. *Physical Review Letters*, 110(26), 265004. <https://doi.org/10.1103/PhysRevLett.110.265004>
- McCubbin, A. J., Howes, G. G., & TenBarge, J. M. (2022). Characterizing velocity-space signatures of electron energization in large-guide-field collisionless magnetic reconnection. *Physics of Plasmas*, 29(5), 052105. <https://doi.org/10.1063/5.0082213>
- Ng, J., Egedal, J., Le, A., Daughton, W., & Chen, L.-J. (2011). Kinetic structure of the electron diffusion region in antiparallel magnetic reconnection. *Physical Review Letters*, 106(6), 065002. <https://doi.org/10.1103/PhysRevLett.106.065002>
- Nicholson, D. R. (1983). *Introduction to plasma theory*. Wiley.
- Pollock, C., Moore, T., Jacques, A., Burch, J., Gliese, U., Saito, Y., et al. (2016). Fast plasma investigation for Magnetospheric Multiscale. *Space Science Reviews*, 199(1), 331–406. <https://doi.org/10.1007/s11214-016-0245-4>
- Roth, M., De Keyser, J., & Kuznetsova, M. M. (1996). Vlasov theory of the equilibrium structure of tangential discontinuities in space plasmas. *Space Science Reviews*, 76(3), 251–317. <https://doi.org/10.1007/BF00197842>
- Russell, C. T., Anderson, B. J., Baumjohann, W., Bromund, K. R., Dearborn, D., Fischer, D., et al. (2016). The magnetospheric multiscale magnetometers. *Space Science Reviews*, 199(1), 189–256. <https://doi.org/10.1007/s11214-014-0057-3>
- Servidio, S., Chasapis, A., Matthaeus, W. H., Perrone, D., Valentini, F., Parashar, T. N., et al. (2017). Magnetospheric Multiscale observation of plasma velocity-space cascade: Hermite representation and theory. *Physical Review Letters*, 119(20), 205101. <https://doi.org/10.1103/PhysRevLett.119.205101>
- Shuster, J. R., Bessho, N., Wang, S., & Ng, J. (2021). Electron-scale temperature gradients in kinetic equilibrium: MMS observations and Vlasov-Maxwell solutions. *Physics of Plasmas*, 28(12), 122902. <https://doi.org/10.1063/5.0069559>
- Shuster, J. R., Chen, L.-J., Daughton, W. S., Lee, L. C., Lee, K. H., Bessho, N., et al. (2014). Highly structured electron anisotropy in collisionless reconnection exhausts. *Geophysical Research Letters*, 41(15), 5389–5395. <https://doi.org/10.1002/2014GL060608>
- Shuster, J. R., Chen, L.-J., Hesse, M., Argall, M. R., Daughton, W., Torbert, R. B., & Bessho, N. (2015). Spatiotemporal evolution of electron characteristics in the electron diffusion region of magnetic reconnection: Implications for acceleration and heating. *Geophysical Research Letters*, 42(8), 2586–2593. <https://doi.org/10.1002/2015GL063601>
- Shuster, J. R., Gershman, D. J., Chen, L.-J., Wang, S., Bessho, N., Dorelli, J. C., et al. (2019). MMS measurements of the Vlasov equation: Probing the electron pressure divergence within thin current sheets. *Geophysical Research Letters*, 46(14), 7862–7872. <https://doi.org/10.1029/2019GL083549>

- Shuster, J. R., Gershman, D. J., Dorelli, J. C., Giles, B. L., Wang, S., Bessho, N., et al. (2021). Structures in the terms of the Vlasov equation observed at Earth's magnetopause. *Nature Physics*, 17(9), 1056–1065. <https://doi.org/10.1038/s41567-021-01280-6>
- Sitnov, M. I., Merkin, V. G., Roytershteyn, V., & Swisdak, M. (2018). Kinetic dissipation around a dipolarization front. *Geophysical Research Letters*, 45(10), 4639–4647. <https://doi.org/10.1029/2018GL077874>
- Stawarz, J. E., Matteini, L., Parashar, T. N., Franci, L., Eastwood, J. P., Gonzalez, C. A., et al. (2021). Comparative analysis of the various generalized Ohm's law terms in magnetosheath turbulence as observed by Magnetospheric Multiscale. *Journal of Geophysical Research: Space Physics*, 126(1), 2020JA028447. <https://doi.org/10.1029/2020JA028447>
- Torbert, R. B., Burch, J. L., Argall, M. R., Alm, L., Farrugia, C. J., Forbes, T. G., et al. (2017). Structure and dissipation characteristics of an electron diffusion region observed by MMS during a rapid, normal-incidence magnetopause crossing. *Journal of Geophysical Research: Space Physics*, 122(12), 11901–11916. <https://doi.org/10.1002/2017JA024579>
- Torbert, R. B., Burch, J. L., Phan, T. D., Hesse, M., Argall, M. R., Shuster, J., et al. (2018). Electron-scale dynamics of the diffusion region during symmetric magnetic reconnection in space. *Science*, 362(6421), 1391–1395. <https://doi.org/10.1126/science.aat2998>
- Vlasov, A. A. (1945). On the kinetic theory of an assembly of particles with collective interaction. *Journal of Physics (USSR)*, 9, 25–40.
- Wang, S., Chen, L.-J., Bessho, N., Hesse, M., Yoo, J., Yamada, M., et al. (2018). Energy conversion and partition in the asymmetric reconnection diffusion region. *Journal of Geophysical Research: Space Physics*, 123(10), 8185–8205. <https://doi.org/10.1029/2018JA025519>
- Wang, S., Chen, L.-J., Bessho, N., Kistler, L. M., Shuster, J. R., & Guo, R. (2016). Electron heating in the exhaust of magnetic reconnection with negligible guide field. *Journal of Geophysical Research: Space Physics*, 121(3), 2104–2130. <https://doi.org/10.1002/2015JA021892>
- Webster, J. M., Burch, J. L., Reiff, P. H., Daou, A. G., Genestreti, K. J., Graham, D. B., et al. (2018). Magnetospheric multiscale dayside reconnection electron diffusion region events. *Journal of Geophysical Research: Space Physics*, 123(6), 4858–4878. <https://doi.org/10.1029/2018JA025245>
- Wilder, F. D., Ergun, R. E., Eriksson, S., Phan, T. D., Burch, J. L., Ahmadi, N., et al. (2017). Multipoint measurements of the electron jet of symmetric magnetic reconnection with a moderate guide field. *Physical Review Letters*, 118(26), 265101. <https://doi.org/10.1103/PhysRevLett.118.265101>
- Yang, Y., Matthaeus, W. H., Parashar, T. N., Haggerty, C. C., Roytershteyn, V., Daughton, W., et al. (2017). Energy transfer, pressure tensor, and heating of kinetic plasma. *Physics of Plasmas*, 24(7), 072306. <https://doi.org/10.1063/1.4990421>